

AD-A115 519

DELAWARE UNIV NEWARK COLL OF MARINE STUDIES
OCEANIC FRONTAL STABILITY: A NUMERICAL MODEL, (U)
NOV 81 W W MARTIN
CMS-02-81

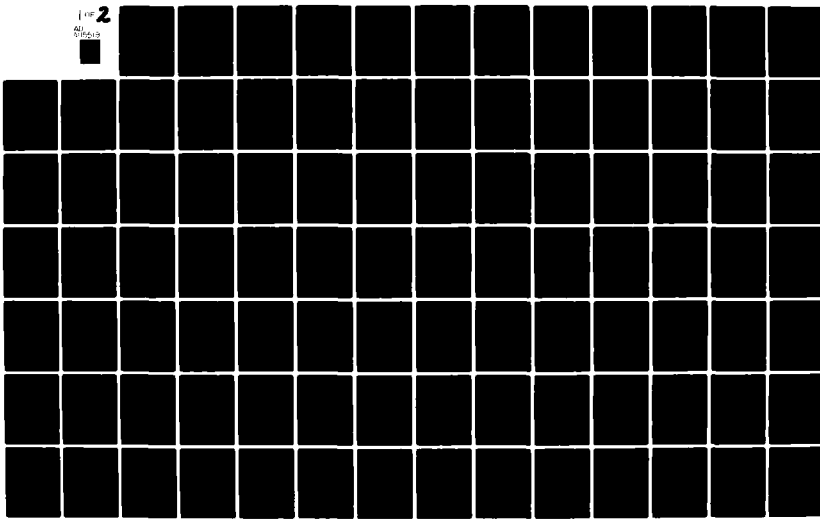
F/6 8/10

N00014-75-C-0714

NL

UNCLASSIFIED

1 of 2
40
010513



卷之三

62

Oceanic Frontal Stability: A Numerical Model

WAYNE W. MARTIN

CMS-02-81

NOVEMBER 1981

APPROVED FOR PUBLIC RELEASE; DISTRIBUTION UNLIMITED

College of Marine Studies • University of Delaware

DRAFT FILE COPY

OCEANIC FRONTAL STABILITY:
A NUMERICAL MODEL

By

Wayne W. Martin

A contract report prepared for
Ocean Science and Technology Division
Office of Naval Research
Contract N00014-75-C-0714

CMS-02-81

November 1981

APPROVED FOR PUBLIC RELEASE; DISTRIBUTION UNLIMITED

College of Marine Studies
University of Delaware
Newark, Delaware 19711



Accession For	
NTIS	GRA&I
DTIC TAB	<input type="checkbox"/>
Unannounced	<input type="checkbox"/>
Justification	
By _____	
Distribution/	
Availability Codes	
Dist	Avail and/or Special
A	

ABSTRACT

A stable, convergent numerical model has been developed to study the evolution of mesoscale meanders of oceanic fronts. A finite difference model was used with the frontal zone divided into two regions, a dissipative zone near the surface expression of the front, and an inviscid region where the frontal interface was deeper. Tests using this model focused on some of the parameters which affect the stability characteristics of these meanders. The parameters studied were: wavelength/Rossby radius ratio, amplitude/wavelength ratio, and cross stream Froude number. Tests were run using oceanographic conditions representative of two regions, the Gulf Stream downstream of Cape Hatteras, and the Sargasso Sea at $30^{\circ}N$.

The model was shown to be sensitive to the wavelength/Rossby radius ratio. For the Sargasso Sea conditions a 30 km disturbance was more stable with respect to amplitude growth than a 100 km disturbance. Both the magnitude and sign of the cross stream Froude number affected the meander stability, with a negative Froude number (downward entrainment near the surface front) showing the greatest amplitude growth. The model results were very sensitive to the meander amplitude. Amplitude growth rates obtained from this model for small amplitude meanders were similar to results from several small amplitude analytic models.

meant for

The growth rates from large amplitude tests were much lower, and closely matched observational results.

This model also showed a tendency toward growing inertial period oscillations near the boundary between the dissipative and inviscid regions. These oscillations were controlled here by interfacial friction. A more accurate representation of the dissipative region may be necessary to properly dissipate the inertial period energy.

ACKNOWLEDGEMENTS

I would like to thank my advisor, Dr. Richard Garvine, who initially suggested this problem and provided numerous valuable technical and editorial suggestions. I would also like to thank Kathy Maas for the illustrations and Sue Thompson for typing the manuscript. This work was supported by the Office of Naval Research under contract N00014-75-C-0714.

TABLE OF CONTENTS

	<u>Page</u>
Introduction.....	1
1.1 Observations of oceanic fronts.....	1
1.2 Frontal models.....	3
 The Eulerian Model.....	 11
2.1 Physical description.....	11
2.2 Initial equation.....	13
2.3 Scaling.....	17
2.4 Conservation form of the equations.....	18
2.5 Interfacial friction.....	20
2.6 Kinetic and potential energy.....	22
2.7 Potential vorticity.....	23
2.8 Conditions on the end boundaries.....	24
2.9 Parent pool boundary condition.....	25
 The Lagrangian Model.....	 27
3.1 Basic equations.....	27
3.2 Mass flux correction.....	28
3.3 Difference equations.....	31

TABLE OF CONTENTS

(continued)

	<u>Page</u>
Initial Conditions.....	32
4.1 Depth.....	32
4.2 Velocity.....	34
Model Testing.....	36
5.1 General description.....	36
5.2 Selection of the coefficient of friction.....	42
5.3 Sensitivity tests.....	43
Model Results.....	49
6.1 Introduction.....	49
6.2 Gulf Stream unperturbed front.....	50
6.3 Gulf Stream small amplitude perturbation.....	55
6.4 Gulf Stream large amplitude perturbation.....	62
6.5 Sargasso Sea short wavelength perturbation.....	74
6.6 Sargasso Sea long wavelength perturbation.....	80
Conclusions.....	87
Appendix I - Computational Implementation.....	94
AI.1 Finite differencing.....	94
AI.2 Smoothing.....	98
AI.3 Extrapolation to inner region points.....	101

TABLE OF CONTENTS

(continued)

	<u>Page</u>
Appendix II - Other Computational Techniques.....	103
AII.1 Depth derivatives at the free boundary.....	103
AII.2 Grid point status determination.....	105
AII.3 Redistribution of points along the boundary.....	108

LIST OF FIGURES

<u>Figure</u>	<u>Title</u>	<u>Page</u>
1	A section in a vertical plane across the front showing the division of the area into the ambient region and the inner and outer frontal regions. The unperturbed surface front lies parallel to the y axis (into the page).	115
2	Plan view of the initial perturbed position of the inner/outer boundary and the surface front, and the position of the inner/outer boundary at a later time after frontal evolution.	116
3	Model grid showing the positions of the boundaries. The dotted line through the solid circles (quasi-Lagrangian drift points) shows the position of the free boundary. The dashed lines show equivalent pairs of grid lines which make the top and bottom boundaries periodic.	117
4	A section of the free boundary showing the velocity components. The component of velocity perpendicular to the front, q_{\perp} , is controlled by the particle velocity, $q_{\perp p}$, and the velocity due to the mass flux, $q_{\perp f}$.	118
5	A section of the free boundary showing the mass flux velocity components. The grid oriented velocities, \hat{u}_f and \hat{v}_f , are components of the flux velocity, q_f , which is equal to the sum of v_p and v_f , the boundary perpendicular and parallel velocities.	119
6	Normalized energy vs. time (in inertial periods) for various values of the friction coefficient: a) 0.001, b) 0.0015, c) 0.002, d) 0.004.	120
7	Losses of a) kinetic energy and b) potential energy due to interfacial friction.	121

LIST OF FIGURES

(continued)

<u>Figure</u>	<u>Title</u>	<u>Page</u>
8	Depth contours for the standard case and two comparison cases. Dashed lines show free boundary position, $\delta = \delta_B = 0.33$. Solid lines are contours at $\delta = 0.4, 0.5, 0.6, 0.7, 0.8$, and 0.9 . The four plots are for: a) initial state, b) grid sensitivity case, c) standard case, d) time step sensitivity case, all cases after ten inertial periods.	122
9	Frontal position vs. time for unperturbed front with varying cross stream Froude numbers. $F_r = -0.02$, $F_r = 0.0$, $F_r = 0.01$ initially at $x = 3.5$, $F_r = 0.01$ initially at $x = 5.5$. Solid symbols and connecting lines show the corresponding linear fits to the frontal positions.	123
10	Cross stream velocity across the frontal region for the unperturbed front after ten inertial periods. The solid line is for $F_r = 0.0$, the dotted line is for $F_r = 0.01$ and the dashed line is for $F_r = -0.02$.	124
11	Time sequence of frontal position. The leftmost curve of each shows the initial disturbance. Time advances to the right with each curve being successively one inertial period later. The x scale for each curve has been expanded by a factor of five to enhance the visibility of the small amplitude perturbations. The three sets are for: a) $F_r = -0.02$, b) $F_r = 0.00$, c) $F_r = 0.01$.	125
12	Depth contours, large amplitude perturbation. The four plots are for a) $F_r = -0.02$, b) $F_r = 0.00$, c) $F_r = 0.01$, and d) $F_r = -0.02$, inverted bulge.	126
13	Time sequence of frontal position, large amplitude disturbance. Time advances to the right. Curves are for 0, 2, 6, and 10 inertial periods.	127
14	Depth contours large amplitude disturbance extended run. Curves are for a) 18 and b) 34 inertial periods.	128

LIST OF FIGURES

(continued)

<u>Figure</u>	<u>Title</u>	<u>Page</u>
15	Normalized kinetic energy vs. time (in inertial periods) for the extended large amplitude disturbance test.	129
16	Spectra obtained from the normalized kinetic energy (Fig. 15). a) 0-14 inertial periods, b) 14-34 inertial periods. Spectral power units are arbitrary due to the original data being normalized.	130 131
17	Time series of frontal position for the Sargasso Sea short wavelength tests, a) $F_r = -0.02$, b) $F_r = 0.00$, c) $F_r = 0.01$. Time advances to the right at one inertial period intervals. The x scale for each curve has been expanded by a factor of five.	132
18	Time sequence of frontal position for the Sargasso Sea long wavelength 3 km amplitude test. Time advances to the right at one inertial period intervals. The x scale for each curve has been expanded by a factor of five.	133
19	Time sequence for the frontal position for the Sargasso Sea long wavelength, 30 km amplitude test. Time advances to the right at one inertial period intervals.	134
20	Depth contours for the Sargasso Sea long wavelength, 30 km amplitude test. Plots are for the initial and final (after ten inertial periods) states.	135
21	Effect of smoothing a) linear profile, b) exponential profile.	136

INTRODUCTION

1.1 - Observations of Oceanic Fronts

Oceanic fronts constitute a boundary between two water masses of different temperature, salinity, and density. The change between the water masses may occur across a distance of a few meters to a few kilometers. The front generally angles downward with a shallow slope (e.g., one in one hundred). As suggested by Stommel (1976), this downward slope often tapers off to give an 'exponential' profile. The abrupt change in physical characteristics across the front has been observed to have a profound effect on the dynamics of the region (Voorhis, 1969; Stommel, 1976), and upon the biota. Backus et al. (1969) found major changes in the biota across a front in the Sargasso Sea. The species composition, total fish population, and primary productivity were all strikingly different on the two sides of the boundary. A cross-frontal shear in the velocity component parallel to the front is often observed, and is often quite intense. In addition, significant surface velocities perpendicular to the front have been observed, and the front is a zone of surface convergence and sinking (Garvine and Monk, 1974; Voorhis, 1969). This convergence collects nutrients, debris, and foam at the surface expression of the frontal interface, often making it highly visible. Other characteristics of the water such as color, turbidity, and surface roughness may change abruptly, thus also enhancing the

visibility of the boundary.

Studies of fronts in the ocean and atmosphere can be divided into three groups, depending upon the stage in the evolution of the front which is examined. There are those studies which are concerned with the generation of fronts, or frontogenesis; those which deal with the behavior of established, persistent fronts; and those involving the dissipation and disappearance of fronts, or frontolysis. For many types of fronts, the frontogenic and frontolytic periods occur in such close apposition that a middle period of enduring existence cannot be defined. However, other types of fronts, such as the Gulf Stream and the atmospheric jet stream, have such a degree of permanence that it is the generative and dissipative periods which do not exist. These semi-permanent fronts can have very active dynamics and often strongly influence the local circulations and energy exchanges.

A major feature of persistent fronts is their tendency to develop meanders, i.e., displacements of the frontal interface away from a straight line. Meanders are most often observed as lateral displacements in the position of the surface expression of the front, forming a wavelike pattern. In western boundary currents such as the Gulf Stream, meanders can grow to such a large amplitude that the bulge breaks off to form a cyclonic or anticyclonic eddy or 'ring'. South of Cape Hatteras the Gulf Stream usually exhibits relatively small amplitude fluctuations. After the Stream's departure from the shelf/slope region north of Cape Hatteras, however, the meanders increase in amplitude and often form eddies south of Georges Bank.

Some of the earliest observations of Gulf Stream meanders were taken during the Multiple Ship Survey of June 1950 (Fuglister and Worthington, 1951). More recent shipborne bathythermograph data from Operation Cabot (Hansen, 1970) resulted in estimates for the dominant wavelength and phase speed of 320 km and 8 cm/sec. These results were confirmed by Halliwell and Mooers (1978) in a study using satellite thermal imagery. This study found the dominant meander mode to have a wavelength of 320 km, a phase speed of 6 cm/sec, and a frequency of 6 cycles per year. Meanders have also been observed along fronts in the Sargasso Sea by Voorhis (1969) and Katz (1969) and along the front of the California Current by Bernstein et al. (1977).

1.2 - Frontal Models

Several theoretical models have been developed to study the motions of established fronts, particularly for the atmospheric case. Modeling of oceanic fronts has not progressed as rapidly, due in part to the difficulty in verification and to the more complex environs of the ocean. An important difference between the atmosphere and the ocean is that the atmospheric density is controlled almost entirely by temperature, while the oceanic density is controlled by both temperature and salinity. However, several atmospheric models capture much of the essential physics of oceanic fronts, so that they are relevant to this discussion.

Stoker (1953) rigorously formulated the full nonlinear problem for the propagation of an atmospheric frontal disturbance. He set up four models with four levels of complexity, from few restrictions to

highly restricted. However, even the least complex (most restricted) model was inherently nonlinear and none of the models could be solved analytically. Since general purpose computers were not available at that time, a numerical approach was not practical either, so no solution was obtained. The assumptions made for the most restricted model included an inviscid, incompressible fluid, no change in the Coriolis parameter with latitude (*f*-plane approximation), initially geostrophic balance across the frontal interface which was assumed to be a planar discontinuity, a continuous pressure field, vertical hydrostatic balance, vanishing fluid velocity relative to the front perpendicular to the front both at the front and well away from the front, and a cold (lower) layer much thinner than the ambient fluid.

Whitham (1953), in a companion paper approached Stoker's most restricted model using the method of characteristics, which permits a graphic type of solution. His solution showed the nonlinear character of disturbance propagation and the tendency toward cyclogenesis. Kasahara et al. (1965) solved Stoker's problem III (slightly less restricted than the problem solved by Whitham) numerically. The problem was solved as a free boundary, initial value problem by using a finite difference scheme. An initially sinusoidal disturbance was shown to propagate along the front from west to east and to result in incipient cyclogenesis.

To achieve solutions to the full nonlinear problem, both Whitham and Kasahara et al. used equations which were a rough approximation to the physical system and then tried to achieve exact solutions. If,

however, an approximate solution to the equations is sought, the equations describing the physical system may be placed under lighter restrictions. The most common approximation technique is perturbation analysis. This method has been very successful in many fields of theoretical and applied physics. The assumption which is required for the use of this method is that the disturbance is a small perturbation on the mean flow (amplitude much smaller than the wavelength). This allows the solution to be expanded in a series, from which the second order and higher terms are dropped, thus leaving a linear problem, rather than a nonlinear one. Often used in conjunction with perturbation methods is Fourier analysis in which the disturbance is assumed to be wavelike and sinusoidal. This method is of particular utility when the frequencies cannot be chosen a priori.

Models which rely on the perturbation method of solution must assume that the meander amplitudes are small. However, prior to occlusion, the amplitudes may exceed the wavelength, and in any case are certainly not small. Perturbation models exclude the nonlinear interactions which must be occurring in the frontal regions by dropping higher order terms in the series expansion. While small amplitude models may well represent the early stages of meander propagation, they necessarily omit much of the essential physics.

One of the first studies to use perturbation analysis for the study of oceanic fronts was that of Duxbury (1963). Duxbury's system included a planar front with a constant velocity shear across it. The model was inviscid with no cross-stream motion in the basic state.

All solutions were dynamically stable, due largely to the neglect of the coupling with the dynamics in the lower layer, as shown by Orlanski (1969). The degree of stability was shown to be dependent upon the Froude number. Orlanski (1968, 1969) derived perturbation models that did show unstable wave modes. The flow of energy in these models was shown to be from the mean potential to the mean kinetic energy component, as expected from large scale turbulence and energy considerations. However, neither of Orlanski's models included the effects of dissipation or cross-stream flow in the initial state.

Hansen (1970) made observations of Gulf Stream meanders by shipborne bathythermograph and compared his observational results with the model results of several authors (Duxbury, 1963; Haurwitz and Panofsky, 1950; Lipps, 1963; Tareev, 1965; and Orlanski, 1969). The results showed that the barotropic models (Haurwitz and Panofsky, Lipps, and Duxbury) were not accurate in selecting the wavelength of the dominant mode. Only the Orlanski model made a good estimate of the phase speed and only the models of Lipps and Tareev estimated the rate of meander spatial growth well. None of the estimates of temporal growth were particularly accurate. Thacker (1976) showed that, depending upon the mean velocity and the velocity shear across the interface, the Gulf Stream can show either predominantly spatial or predominantly temporal growth.

Since these models made consistently poor estimates of certain important quantities, some fundamental physics must be missing in their formulations. Possibilities for improvement include: the use of a

dissipation mechanism such as friction, cross-stream flow in the basic state, and the easing of the small amplitude restriction.

In studies of large scale oceanic processes the fluid is often assumed to be inviscid. However, this may not be valid for frontal dynamics. Grammeltvedt (1970) in a numerical solution of the problem considered by Kasahara et al. (1965) (and proposed by Stoker, 1953) showed the development of asymmetries leading to occlusion and eddy formation. However, to maintain numerical stability, the artifice of a dissipative mechanism had to be introduced. Assaf (1977), in an extension of an earlier model by Charney for the Florida Current, produced a cyclonic shear zone by using vertical (interfacial) friction rather than lateral friction. He also showed that friction may act to increase the available potential energy in the Sargasso Sea. It is also apparent that friction generated by a velocity shear at a boundary would be more important where the fluid layer is thin than where it is deep. Thus, it appears that some dissipative mechanism (such as friction) is important to the dynamics of the front, particularly near the surface front.

To show the importance of cross-frontal motions, Saltzman and Tang (1975) derived an analytical model of an atmospheric front. They showed that in the upper troposphere (mid-depth in an oceanic front) there is a horizontal convergence upstream and a divergence downstream of a meander trough, resulting in a non-zero cross front flow. The results indicate that second order, ageostrophic effects can modify a two layer flow. The implication is that asymmetric features such as

frontal meanders are the result of a large scale baroclinic instability with second order effects superposed near the surface front. Thus, there may be two flow regimes, one encompassing the entire frontal region and one active only near the surface front. In another atmospheric frontal model, Orlanski and Ross (1977) showed that a cross-stream circulation could be caused by an ageostrophic residue from the vertical shear of the horizontal velocity and the horizontal gradient of the temperature. In this model the cross-stream motion was required so that the steady state would be maintained. Newton (1978) showed that mid-tropospheric fronts (such as the jet stream) have more similarities to oceanic fronts than do the lower tropospheric fronts which intersect the ground. He discussed analogies between mid-tropospheric and oceanic fronts and derived a model for the effects of confluence on the circulation of an oceanic frontal region. The concentration of horizontal gradients due to confluence in meander motions was shown to cause a sinking at mid-depths and a convergence at the surface in meander troughs, so that the isopycnals become closer in the troughs. This agrees with the results of Saltzman and Tang (1975) and is supported by limited observation for atmospheric fronts. Formato (1979), in a model which explicitly includes frictional dissipation near the surface front, showed that the cross-stream flow is non-zero both in the steady state and in the presence of meanders. Thus, cross-stream motions are an important and perhaps essential component of the frontal dynamics.

Garvine (1974) derived a model for a small scale, steady state oceanic front which included friction and mass entrainment. These

mechanisms were shown to be required at small scales for the maintenance of a steady state. This model was extended (Garvine 1979a; 1979b) to include the rotational (Coriolis) effects present in larger scale fronts. This model was hydrodynamic (density field not determined by model processes), vertically integrated, and used bulk parameterizations for quantities such as friction. An important result of these papers was the derivation of the rotation parameter, which expresses the relative importance of the rotational effects to the effects of friction. Small values indicate that frictional effects are dominant. A value of zero reduced the 1979 model to the 1974 case. For large scale fronts, such as the Gulf Stream, the rotation parameter is large so that rotational effects are dominant for the front as a whole. Garvine demonstrated that dissipation processes are important only for a distance of 10% to 20% of the baroclinic Rossby radius (the cross-stream scale of the frontal system) away from the surface front. However, due to mass entrainment and mixing in this area the entire frontal zone is affected by a cross-stream mass flux.

To improve upon present models, three factors should be considered: a dissipative mechanism such as friction which is active near the surface expression of the front, motion perpendicular to the front in the upper (lighter) layer, and the nonlinear effects of finite amplitude meanders. The intent of this paper is to present a model of an upper ocean density front which specifically addresses the three aforementioned considerations. This model is based on the work of Kasahara et al., but is altered according to the results of Garvine

and Formato. The Kasahara et al. atmospheric front model allows for the full nonlinear equations, and the modifications introduced here add dissipation near the surface front and cross stream mass flux.

The present model is a conjunction of two models. A fixed grid Eulerian model is used for the main portion of the flow and is constrained by three fixed boundaries at which standard boundary conditions are applied. However, the fourth boundary, the front, must be free, a condition which an Eulerian model cannot deal with directly. To accurately compute the behavior of the front, a second, Lagrangian, model is used along the front. The Eulerian grid space provides the acceleration terms for the Lagrangian model through the gradient of the interfacial depth. The results along the free boundary are used at each time step to form a boundary condition for the Eulerian model. The two models thus complement each other and are integrated in parallel through time to describe the time evolution of the flow.

THE EULERIAN MODEL

2.1 - Physical Description

To model an upper ocean density front we assume an incompressible, hydrostatic fluid on a rotating earth. The flow is assumed to be periodic along the direction of the primary flow. The periodicity is imposed by the boundary conditions and the length scale is thus equal to the length of the model grid. The upper surface of the fluid is flat and rigid. A two layer system is used with the upper layer divided into two regions, dissipative and inviscid. Figure 1 shows a vertical section across the front to illustrate the division of the flow field. The lower layer, with the greatest volume, is called the ambient water and lies below and to the left of the frontal (pycnocline) interface. The characteristic depth is h and the density is taken to be uniform at ρ_∞ . The other two regions are comprised of lighter water and lie above the interface. One region is the outer (inviscid) zone where the density is uniform at $\rho_\infty - \Delta\rho$. The depth of the interface is D , and varies in space and time. Since the flow in this region has been taken to be inviscid, there is no vertical shear in the horizontal velocity components, u and v . To the right of the inviscid region of the front is a reservoir of light water, called the parent pool, where the depth and velocity remain unaffected by any variations in the motion in the frontal zone. The horizontal scale of the entire frontal

zone is the baroclinic Rossby radius, $\lambda = c/f$. Here c is the internal wave speed, $c = (g'D_0)^{1/2}$, where $g' = \frac{\Delta\rho}{\rho_\infty} g$, the reduced gravity and D_0 is the depth of the pycnocline in the parent pool. The Coriolis parameter is f , and is taken to be constant with latitude (f -plane approximation).

The second region above the interface is the dissipative zone. This region adjoins the surface front and extends away from it for a distance of 10% to 20% of λ . The primary importance of the inner region is its influence on the outer region at the common juncture. The assumed high level of turbulence in the inner region permits the use of a local, quasi-steady solution, because the time scale there for flow adjustments to changes in the boundary conditions is short compared to the time scale for the outer region. In the model the inner (dissipative) region is treated as a 'grey box'. Some of the details of the turbulent processes occurring inside of it are known, but not enough for it to be modeled accurately at a level compatible with this modeling effort. Therefore, the inner region is assumed to be a source or sink of water for the outer region, but the details of the flow are not modeled.

We assume that D/h is small which permits great simplification in the dynamics, since the motion in the ambient layer is then uncoupled from that above the interface (Garvine, 1979a), and will be assumed to be in uniform geostrophic balance. This means that above the pycnocline, including the dissipative zone, the flow will be in isostatic balance. This also allows us to reduce the computation to a one layer, reduced gravity model.

Figure 2 shows the coordinate system to be used in the horizontal plane. In the basic or unperturbed state, the surface front lies parallel to the y-axis. The positive x-axis points towards the light water reservoir, and the z-axis is upwards. This coordinate system is similar to that used by Formato. Here, however, the perturbations to the front will not be decomposed into steady state and perturbation components. A horizontal perturbation may be applied to the inner/outer boundary with an amplitude to wavelength ratio between zero (straight or unperturbed) to order one. The perturbation is applied as a cosine shaped disturbance.

2.2 - Initial Equations

The system of equations governing the inviscid region are well known. Listed in order of vertically integrated continuity, x momentum, and y momentum they are, for an earth fixed coordinate system:

$$\partial_{t^*} + (u^* \partial)_{x^*} + (v^* \partial)_{y^*} = 0 \quad (2.2.1)$$

$$u_{t^*}^* + u^* u_{x^*}^* + v^* u_{y^*}^* - f_{v^*} = -\frac{1}{\rho} p_{x^*} \quad (2.2.2)$$

$$v_{t^*}^* + u^* v_{x^*}^* + v^* v_{y^*}^* + f_{u^*} = -\frac{1}{\rho} p_{y^*} \quad (2.2.3)$$

These equations are the same as those for large amplitude (nonlinear) long internal waves, including the effects of the earth's rotation. For the non-rotational case ($f = 0$), they are identical to the nonlinear shallow water wave equations, with ∂ analogous to the surface height. The system is thus hyperbolic and has real character-

istics. As is well known, such wave systems are often found in nature with hydraulic jumps at their advancing boundaries (Stoker, 1957).

Tidal bores are a common example. In this case the dissipative region is directly analogous to the shallow water bore and the inviscid region is analogous to the long wave region behind the bore.

For generality we include a transformation to a coordinate system which is moving with the speed of the unperturbed portion of the front. This will allow the separation of the linear frontal propagation from the frontal meandering. A simple Galilean transformation is

$$\left. \begin{array}{l} x' = x^* - U_f t^* \\ y' = y^* - V_f t^* \\ t' = t^* \\ u' = u^* - U_f \\ v' = v^* - V_f \end{array} \right\} \quad (2.2.4)$$

where U_f and V_f are the frontal propagation velocities. This leads to

$$D_{t'} + (u'D)_{x'} + (v'D)_{y'} = 0 \quad (2.2.5)$$

$$u'_{t'} + u'u'_{x'} + v'u'_{y'} - f(v' + V_f) = -\frac{1}{\sigma} p_x' \quad (2.2.6)$$

$$u'_{t'} + u'v'_{x'} + v'v'_{y'} + f(u' + U_f) = -\frac{1}{\sigma} p_y' \quad (2.2.7)$$

The pressure terms on the right hand side will be difficult to work with in this type of model. An easier variable to use is the interfacial depth. Since the upper layer is homogeneous and in isostatic balance, this conversion may be made by calculating the pressure field hydrostatically.

$$p = g(\rho_\infty - \Delta\rho)(n - z) \quad -D \leq z \leq n \quad (2.2.8)$$

$$p = g\{(\rho_\infty - \Delta\rho)n - (\rho_\infty z + \Delta\rho D)\} \quad z \leq -D \quad (2.2.9)$$

Neglecting terms of order $\frac{\Delta\rho}{\rho_\infty}$ compared to unity, the hydrostatic pressure gradient is

$$\nabla_h \frac{p}{\rho_\infty} = g\nabla_h n \quad -D \leq z \leq n \quad (2.2.10)$$

$$\nabla_h \frac{p}{\rho_\infty} = g\nabla_h n \left(n - \frac{\Delta\rho}{\rho_\infty} D\right) \quad z \leq -D \quad (2.2.11)$$

Below the interface, in the ambient fluid region, the hydrostatic pressure gradient is balanced geostrophically. Setting U_a , V_a as the ambient fluid velocities, we have

$$g\nabla_h \left(n - \frac{\Delta\rho}{\rho_\infty} D\right) = f V_a \vec{i} - f U_a \vec{j} \quad (2.2.12)$$

Performing the Galilean transformations as above

$$\left. \begin{aligned} u'_\infty &= U_a - U_f \\ v'_\infty &= V_a - V_f \end{aligned} \right\} \quad (2.2.13)$$

so that

$$g\nabla_h n - g \frac{\Delta\rho}{\rho_\infty} \nabla_h D = f(v_\infty + v_f) \vec{i} - f(u_\infty - U_f) \vec{j} \quad (2.2.14)$$

Using the reduced gravity $g' = \frac{\Delta\rho}{\rho_\infty} g$ above the interface

$$\begin{aligned} \nabla_h \frac{\Delta\rho}{\rho_\infty} &= g\nabla_h n = g' \nabla_h D + f(v_\infty + v_f) \vec{i} \\ &\quad - f(u_\infty + U_f) \vec{j} \end{aligned} \quad (2.2.15)$$

so that (2.2.6) and (2.2.7) become

$$\begin{aligned} u'_t + u'u'_x + v'u'_y - fv' + v_f &= -gD_x, \\ -fv_\infty - \bar{v}v_f & \end{aligned} \quad (2.2.16)$$

$$\begin{aligned} v'_t + u'v'_x + v'v'_y + fu' + U_f &= -gD_y, \\ -fu_\infty + fU_f & \end{aligned} \quad (2.2.17)$$

The basic equations for the system are

$$u'_t + u'u'_x + v'u'_y - fv' = -g'D_x - fv'_\infty \quad (2.2.18)$$

$$v'_t + u'v'_x + v'v'_y + fu' = -g'D_y + fu'_\infty \quad (2.2.19)$$

$$D_t + (u'D)_x + (v'D)_y = 0 \quad (2.2.20)$$

2.3 - Scaling

For convenience the basic equations (2.2.18)-(2.2.20) will now be put into non-dimensional form. The primary assumptions made in this scaling are that the velocity scale is the internal wave speed $C = (g'D_0)^{1/2}$ and the length scale is the baroclinic Rossby radius of deformation $\lambda = \frac{C}{f}$. The obvious time scale is then based on the inertial frequency, f. With these scales, the variable transformations are

$$\left. \begin{array}{ll} x = \lambda \eta & u' = u \lambda f \\ y = \lambda \zeta & v' = v \lambda f \\ t = \tau/f & u'_\infty = u_\infty \lambda f \\ D = \delta D_0 & v'_\infty = v_\infty \lambda f \\ g'D = \delta (f\lambda)^2 & \end{array} \right\} \quad (2.3.1)$$

Note that the internal cross stream Froude number $F_r = \frac{u'_0}{C}$ which is equal to u_0 , the parent pool cross stream velocity.

Using these equations (2.2.18) becomes

$$\begin{aligned} f \frac{\partial}{\partial \tau} (uf\lambda) + uf\lambda \frac{1}{\lambda} \frac{\partial}{\partial \eta} (uf\lambda) + vf\lambda \frac{\partial}{\partial \zeta} (uf\lambda) \\ - f(vf\lambda) = - \frac{1}{\lambda} \frac{\partial}{\partial \eta} (\partial f^2 \lambda^2) - f(v_\infty f\lambda) \end{aligned} \quad (2.3.2)$$

Multiplying by $\frac{1}{f^2 \lambda}$ yields

$$u_\tau + uu_n + vu_\zeta - v = -\delta_n - v_\infty \quad (2.3.3)$$

Equation (2.2.19) is, similarly

$$v_\tau + uv_n + vv_\zeta + u = -\delta_n + u_\infty \quad (2.3.4)$$

With the new variables equation (2.2.20) is

$$\delta_\tau = -u\delta_n - \delta u_n - v\delta_\zeta - \delta v_\zeta \quad (2.3.5)$$

2.4 - Conservation form of the equations

The difference scheme to be used requires that the initial equations be in conservation form (see appendix I). This means that they must be in the form

$$w_t = f_x + g_y + z \quad (2.4.1)$$

where w is a vector containing the three dependent variables. The vectors f and g are functions of w which are differentiated in space, and z is a vector containing the inhomogeneous terms. Equation (2.3.5) is already in this form and equations (2.3.3) and (2.3.4) may be transformed by converting to mass flux variables instead of the velocity terms. Multiplying (2.3.3) by δ

$$\delta u_\tau + \delta uu_n + \delta vv_\zeta - \delta v = -\delta \delta_n - \delta v_\infty \quad (2.4.2)$$

and multiplying (2.3.3) by u

$$u\delta_\tau + u^2\delta_n + \delta uu_n + uv\delta_\zeta + \delta uv_\zeta = 0 \quad (2.4.3)$$

and adding the two

$$\begin{aligned} \delta u_\tau + u \delta_\tau + \delta uu_\eta + \delta uu_\eta + u^2 \delta_\eta + \delta \delta_\eta + uv \delta_\zeta \\ + \delta uv_\zeta + \delta vu_\zeta - \delta v + \delta v_\infty = 0 \end{aligned}$$

or

$$(\delta u)_\tau = - \left[\frac{(\delta u)^2}{\delta} \right]_\eta - \left[\frac{1}{2} \delta^2 \right]_\eta - \left[\frac{\delta u \delta v}{\delta} \right]_\zeta + \delta v - \delta v_\infty \quad (2.4.4)$$

Similarly we may multiply (2.3.4) by δ and (2.3.5) by v and add the two to give

$$\begin{aligned} \delta v_\tau + v \delta_\tau + \delta uv_\eta + \delta vu_\eta + uv \delta_\eta + 2 \delta vv_\eta \\ + v^2 \delta_\zeta + \delta \delta_\zeta + \delta u - \delta u_\infty = 0 \end{aligned}$$

or,

$$(\delta v)_\tau = - \left[\frac{\delta u \delta v}{\delta} \right]_\eta - \left[\frac{(\delta v)^2}{\delta} \right]_\zeta - \left[\frac{1}{2} \delta^2 \right]_\zeta - \delta u - \delta u_\infty \quad (2.4.5)$$

If we let $\phi = \delta u$, and $\psi = \delta v$ equations (2.4.4), (2.4.5), and (2.3.5) become

$$\phi_\tau = - \left[\frac{\phi^2}{\delta} + \frac{1}{2} \delta^2 \right]_\eta + \left[\frac{\phi \psi}{\delta} \right]_\zeta + \psi - \delta v_\infty \quad (2.4.6)$$

$$\psi_\tau = -\left(\frac{\phi\psi}{\delta}\right)_n - \left(\frac{\psi^2}{\delta} + \frac{1}{2}\delta^2\right)_\zeta - \phi + \delta u_\infty \quad (2.4.7)$$

$$\delta_\tau = -\phi_n - \psi_\zeta \quad (2.4.8)$$

or

$$w_\tau = f(w)_n + g(w)_\zeta + z \quad (2.4.9)$$

where

$$w = \begin{Bmatrix} \phi \\ \psi \\ \delta \end{Bmatrix} \quad f = \begin{Bmatrix} \frac{\phi^2}{\delta} + \frac{1}{2}\delta^2 \\ \frac{\phi\psi}{\delta} \\ \phi \end{Bmatrix} \quad (2.4.10)$$

$$g = \begin{Bmatrix} \frac{\phi\psi}{\delta} \\ \frac{\psi^2}{\delta} + \frac{1}{2}\delta^2 \\ \psi \end{Bmatrix} \quad z = \begin{Bmatrix} \psi - \delta v_\infty \\ -\phi + \delta u_\infty \\ 0 \end{Bmatrix}$$

This is the form of the equations that will be inserted into the finite differencing scheme for the fixed grid portion of the flow.

2.5 - Interfacial friction

Although the outer region is modeled as an inviscid fluid there will be some frictional effects, primarily at the interface between the water in the outer region and the ambient water. This friction may be

characterized by a bulk stress formula

$$F'_D = C'_D v' |v'| \quad (2.5.1)$$

where F'_D is the frictional drag force and C'_D is the coefficient of friction. Note that F'_D is proportional to the square of the velocity, although the absolute value form is used here to orient the drag force properly with respect to the velocity. The coefficient of drag must be scaled in the same manner as the main equations were in section 2.3.

Using the velocity scaling we have:

$$F_D \lambda f^2 = C_D \frac{1}{\lambda} v |v| \lambda^2 f^2$$

or

$$F_D = C_D v |v| \quad (2.5.2)$$

The use of interfacial drag provides a simple method for including the effect of local instabilities of high frequency internal gravity waves propagating along the interface. It also stabilizes the model by reducing the inertial oscillations which occur as a result of imperfect initial conditions and which can amplify if not suppressed.

The friction in this model is not treated as operating within the upper layer, but only at the interface, and is described by a bulk parametrization. Therefore, it is not included in the initial momentum equations (2.2.2-2.2.3) and is thus excluded from the results of the finite difference computations. The calculation of friction is appended

to the differencing as an auxiliary operation, along with the adjustments for the boundary conditions discussed in sections 2.8 and 2.9.

2.6 - Kinetic and potential energy

The behavior of the model in the outer region will be followed by the time and space evolution of the three independent variables; depth and the two components of velocity. The spatially integrated kinetic and potential energies will also be computed to assist in the physical interpretation of the model results. The equations for the kinetic and potential energies spatially summed over the outer region are:

$$K.E. = \frac{1}{2} \sum_n \sum_{\zeta} (u'^2 + v'^2) D \quad (2.6.1)$$

$$P.E. = \frac{1}{2} g' \sum_n \sum_{\zeta} D^2 \quad (2.6.2)$$

Scaling these as in section 2.3:

$$K.E. = \frac{1}{2} D_0 c^2 \sum_n \sum_{\zeta} (u^2 + v^2) \delta \quad (2.6.3)$$

$$P.E. = \frac{1}{2} (\lambda f)^2 \sum_n \sum_{\zeta} \delta^2 \quad (2.6.4)$$

Following Orlanski and Cox (1973) these are divided into mean and perturbation components. Horizontal means are taken in the along frontal direction for each of the three basic variables as:

$$\bar{u}(x,t) = \frac{1}{N} \int_0^N u(x,y,t) dy \quad (2.6.5)$$

and the perturbation quantities as:

$$u'(x,y,t) = u(x,y,t) - \bar{u}(x,t) \quad (2.6.6)$$

From the mean and perturbation components of the three independent variables, the mean and perturbation components of the kinetic and potential energies are computed by equations (2.6.3) and (2.6.4). The results of these calculations will indicate the directions and relative rates of the energy transformations. These will be diagnostic of the stability characteristics of the perturbations to the flow.

2.7 - Potential vorticity

In the investigation of wave phenomena it is sometimes useful to employ a vorticity equation. Such an equation may be easily derived for this case. By cross differentiating (2.2.18) and (2.2.19) and then subtracting, the terms involving δ may be eliminated. Setting the vorticity as $\gamma = v_n - u_\zeta$, we have

$$\gamma_\tau + (u\gamma_n) + (v\gamma)_\zeta + u_n + v_\zeta = 0 \quad (2.7.1)$$

or

$$\gamma_\tau + (u\gamma + u)_n + (v\gamma + v)_\zeta = 0 \quad (2.7.2)$$

By combining this equation with continuity (2.2.20), we may derive an equation for the conservation of potential vorticity:

$$\frac{D}{D\tau} \left(\frac{\chi + 1}{\delta} \right) = 0 \quad (2.7.3)$$

In analytical models such an equation is often substituted for one of the momentum equations in the set of initial equations. In this case the vorticity equation does not fit into the differencing scheme and attempts to circumvent the problem by a spatial integration were unsuccessful.

The potential vorticity equation is still useful, however, in checking the results of the model. The potential vorticity at each grid point may be calculated from (2.7.2) and displayed graphically. Since the potential vorticity field is originally uniform from the initial conditions, and since the outer region is inviscid, except as discussed in section 2.5, the uniformity of the field at later points in time is a test of the stability and accuracy of the model.

2.8 - Conditions on the end boundaries

Since the finite difference scheme can cover only a limited region of space along the front, boundary conditions must be applied along lines perpendicular to the front at the ends of the grid space (the 'top' and 'bottom' boundaries in Fig. 3). It is assumed that these edges are far away relative to the disturbance of interest so that the exact form of the conditions will not be critical to the performance of the model. For ease of implementation a periodic boundary condition is used. That is, each edge becomes a neighbor to the other for the computation of derivatives and mass flux terms.

To implement the periodic boundary condition and to provide sufficient grid overlap for the determination of the depth derivatives (see Appendix II), the bottom three grid lines are repeated at the top of the grid. In the notation of Fig. 3, the grid points along the grid line at $N-2$ are the same as those along the line at 1. The lines at 2 and $N-1$, and at 3 and N also form equivalent pairs. The front points are also subject to the periodic boundary condition. This is important primarily for smoothing. When a front point moves above a limit at the 'top' edge, it is moved to the 'bottom' of the grid, as though it were just entering the grid from the bottom.

2.9 - Parent Pool Boundary Condition

The parent pool region is assumed to be undisturbed by the motions of the front. The depth is constant at D_0 , the scaling depth, so that $\delta = 1$. The v velocity is zero since the parent pool and ambient waters are assumed to have no relative motion. The u velocity component compensates (approximately) for the mass entrainment in the frontal region. Derivatives of all of the variables are assumed to vanish in the parent pool.

These conditions are applied to the model boundary along the parent pool as initial conditions. However, they cannot be used as fixed boundary conditions at later time steps. If the boundary values are held at fixed levels, disturbances which are generated in the interior of the grid will not be able to escape the domain, but will be reflected or trapped by the boundary. A boundary condition which allows distur-

bances to propagate freely out of the domain is required. As discussed in section 2.8, this problem is solved for the end boundaries through the use of a periodic boundary condition. For the parent pool boundary, however, there is no other boundary available with which to form the periodic condition. A Sommerfeld radiation condition is used instead. This condition may be expressed:

$$\mu_t + c\mu_x = 0$$

where μ is any variable and c is the phase velocity of the waves.

Orlanski (1976) suggests an algorithm for this condition which is employed here. This method consists of two steps. First, for each variable a disturbance phase speed is calculated at each boundary point from the neighboring points in the grid interior. The values of the variables along the boundary are then extrapolated from the neighboring points, using the calculated phase speeds. If the calculated phase speed exceeds the maximum internal wave speed, it is reset to equal the internal wave speed. Similarly, negative calculated phase speeds (disturbances moving away from the boundary) are reset to zero.

THE LAGRANGIAN MODEL

3.1 - Basic Equations

Since the details of the flow in the turbulent inner region are not known, the movement of the surface expression of the front cannot be determined directly. We may infer the frontal position from the position of the boundary between the inner and outer regions by assuming that the configuration of the inner region in the cross frontal direction is not affected by the movement of the boundary. Since one of the major objectives of this research is to follow the time evolution of the front, modeling the inner/outer region boundary is of great importance. Differential equations may be written describing the movement of the free boundary and a differencing scheme must be applied in order to integrate the equations through time. Since an Eulerian approach does not work well for free boundaries, we link a Lagrangian model for this boundary to the Eulerian model for the outer region.

The position of the inner/outer boundary is marked by a series of quasi-Lagrangian drift points. These points are initially set slightly closer together than the spacing of the fixed grid. The initial conditions of frontal disturbance wavelength and amplitude also determine the initial positions of the points along the grid. These drift points are Lagrangian in that their velocities are determined from

the Lagrangian flow equations. However, their motion is determined not only by the Lagrangian velocities, but by the mass flux across the boundary as shown in Fig. 4. The drift points move with the boundary, defining its position. They do not stay with the initial water parcels as fully Lagrangian drifters would, except in the case of zero mass flux across the boundary.

Along the inner/outer boundary the depth of the interface is held constant, $D = D_b$. Non-dimensionally this is

$$\begin{aligned}\delta_b &= g'D_b \left(\frac{1}{f\lambda}\right)^2 \\ &= g'D_b \frac{1}{f^2} \frac{f^2}{g'D_0} \\ &= \frac{D_b}{D_0}\end{aligned}\tag{3.1.1}$$

A fluid particle which is initially on the boundary will move as a Lagrangian drifter in the velocity field. That is, the displacement through time will be

$$\frac{d}{dt}(x_p(t)) = u_p(x_p, y_p, t)\tag{3.1.2a}$$

$$\frac{d}{dt}(y_p(t)) = v_p(x_p, y_p, t)\tag{3.1.2b}$$

3.2 - Mass Flux Correction

If the fluid parcel were to remain on the line defining the boundary, the equations (3.1.2) would describe the displacement of the

boundary. However, turbulent entrainment may occur in the inner region, resulting in a net gain (or loss) of water in that region. If the volume of water in the inner region is to remain constant, then the inner/outer boundary must move with respect to the local water at a velocity which compensates for the entrainment. If, in a unit of time a volume V is entrained into a section of the inner region of unit width, then the velocity of the boundary relative to the water must be

$$v_r = \frac{V}{\delta_b} \quad (3.2.1)$$

We note that there may also be a velocity shear applied to the boundary. This shear velocity, v_λ , will displace water parcels from a point fixed on the boundary in the same manner as the entrainment velocity, v_r . Since the boundary may be curved and not aligned with the model grid, a transformation is required to relate v_r and v_λ to the velocities, \hat{u}_f and \hat{v}_f , which are aligned with the grid and are determined by

$$\hat{u}_f = v_r \cos \theta_n - v_\lambda \sin \theta_n \quad (3.2.2a)$$

$$\hat{v}_f = v_r \sin \theta_n + v_\lambda \cos \theta_n \quad (3.2.2b)$$

This relation is shown graphically in Fig. 5. The instantaneous velocity of a point which is fixed on the boundary will be equal to the velocity of a water parcel on the boundary plus the velocity of the boundary with respect to the water.

$$u_b = u - \hat{u}_f \quad (3.2.3a)$$

$$v_b = v - \hat{v}_f \quad (3.2.3b)$$

If small displacements are assumed, this Eulerian scheme may be linked to a Lagrangian scheme to give the displacements in time of the boundary points

$$\frac{d}{dt}(x_b(t)) = u_p(x_p, y_p, t) - \hat{u}_f \quad (3.2.4a)$$

$$\frac{d}{dt}(y_b(t)) = v_p(x_p, y_p, t) - \hat{v}_f \quad (3.2.4b)$$

In the small time increments involved in the finite difference method of the model, the small displacement condition can easily be met. Since the depth field is available as a boundary condition at the boundary and as a model result on the model grid in the outer region and from extrapolations into the inner region from the boundary (see Appendix I), the u_p and v_p values may be obtained from the momentum equations

$$u_{p\tau} + u_p u_{pn} + v_p u_{p\zeta} - v_p = -\delta_n - v_\infty \quad (3.2.5a)$$

$$v_{p\tau} + u_p v_{pn} + v_p v_{p\zeta} + u_p = -\delta_\zeta + u_\infty \quad (3.2.5b)$$

or,

$$\frac{du_p}{d\tau} = v_p - v_\infty - \delta_n \quad (3.2.6a)$$

$$\frac{dv_p}{d\tau} = -u_p + u_\infty - \delta_\zeta \quad (3.2.6b)$$

3.3 - Difference Equations

To fit the general differencing cycle of the overall model, the momentum and displacement equations must be put into a difference form. The difference forms of (3.2.6) are

$$u_p(\tau + \Delta\tau) = u_p(\tau) + \Delta\tau(v_p - v_\infty - \delta_n) \quad (3.3.1a)$$

$$v_p(\tau + \Delta\tau) = v_p(\tau) + \Delta\tau(-u_p + u_\infty - \delta_\zeta) \quad (3.3.1b)$$

This gives the Lagrangian velocity of the water along the boundary. The motion of the drift points from (3.2.4) is

$$x_b(\tau + \Delta\tau) = x_b(\tau) + \Delta\tau(u_p - \hat{u}_f) \quad (3.3.2a)$$

$$y_b(\tau + \Delta\tau) = y_b(\tau) + \Delta\tau(v_p - \hat{v}_f) \quad (3.3.2b)$$

This formula, applied to each point gives its position on the fixed grid at each time step. These difference equations are solved by a predictor-corrector scheme. The time step used is the same as that used in the finite differencing scheme for the fixed grid, so that the two solutions can advance stepwise in parallel through time.

INITIAL CONDITIONS

4.1 - Depth

Following Formato (1979), we may derive the form of the depth profile from (2.3.3), (2.7.3), and (2.3.6). To find the basic equilibrium state we first eliminate time derivatives. Then, taking y derivatives to be small when compared to x derivatives, we set $u_\zeta = v_\zeta = 0$. The x momentum, vorticity, and continuity equations are then

$$uu_n - v + \delta_n = 0 \quad (4.1.1)$$

$$\left(\frac{v_n + 1}{\delta} \right)_n = 0 \quad (4.1.2)$$

$$(u\delta)_n = 0 \quad (4.1.3)$$

Equations (4.1.2) and (4.1.3) may be integrated to yield

$$v_n + 1 = \delta \quad (4.1.4)$$

$$u\delta = u_0 \quad (4.1.5)$$

Differentiating (4.1.1) with respect to n and substituting for v_n from (4.1.4) and for u from (4.1.5) gives an equation for δ alone,

$$\delta_{nn} \left(1 - \frac{u_0^2}{\delta^3} \right) + \delta^2 \left(3 \frac{u_0^2}{\delta^4} \right) - \delta + 1 = 0 \quad (4.1.6)$$

An exact solution may be obtained for this equation, but the solution is transcendental. However, by noting that $u_0 = F_r$, the cross stream Froude number and requiring $F_r^2 \ll \delta_0 \leq 1$, we may form a small perturbation expansion of the form

$$\delta(n) = \delta^{(0)}(n) + F_r^2 \delta^{(2)}(n) + \dots \quad (4.1.7)$$

Applying (4.1.7) to (4.1.6), we have for the lowest order solution

$$\delta_{nn}^{(0)} - \delta^{(0)} + 1 = 0 \quad (4.1.8)$$

We introduce a new coordinate in the x direction $n_s = (n - n_b)/R_0$, where n_b is the location of the inner/outer boundary and R_0 is the baroclinic Rossby radius. At the boundary $n_s = 0$. The boundary conditions to be met are

$$\delta^{(0)}(n_s = 0) = \delta_b \quad (4.1.9a)$$

$$\lim_{n_s \rightarrow \infty} \delta^{(0)}(n_s) = 1 \quad (4.1.9b)$$

Subject to these conditions the solution of (4.1.8) is

$$\delta(n_s) = 1 - (1 - \delta_b)e^{-n_s} \quad (4.1.10)$$

This gives depth as a function of x directed distance from the front. It is the exponential relation derived by Stommel (1976).

4.2 - Velocity

An expression for the u component of velocity may be obtained directly from (4.1.5)

$$u = \frac{u_0}{\delta} \quad (4.2.1)$$

This expresses cross stream conservation of mass. At the parent pool boundary $u = u_0 = F_r$, and at the free boundary $u = u_0/\delta_b$.

In (4.1.1) the first term will be small by a factor of F_r^2 so that it may be neglected to lowest order. The v component of velocity from this is

$$v = \delta_n \quad (4.2.2)$$

The initial conditions thus include geostrophic balance for the v component. Using the relation for the depth given above, (4.2.2) may be expressed in a slightly different form. Differentiating (4.1.10)

$$\delta_n = (1 - \delta_b)e^{-\eta s} \quad (4.2.3)$$

or

$$\delta_n = 1 - \delta \quad (4.2.4)$$

so that

$$v = 1 - \delta \quad (4.2.5)$$

This relation will be useful later in deriving a smoothing scheme (Appendix I).

MODEL TESTING

5.1 - General Description

The model described above and in the Appendices was coded in FORTRAN and run on a DEC-10 computer at the University of Delaware. After a set of parameters was chosen, the initial conditions were computed and the model was run for one time step with the free boundary held in a fixed position and the solutions in the inner region held at the initial values. This was done to allow for any minor adjustments to the initial conditions necessary in the outer region. Following this initialization, the model runs were executed piecewise; that is, the model was run for one or more inertial periods, the results were examined, and the execution was resumed, continuing for one (or more) inertial periods(s) from the point at which it had been halted. This pattern was repeated until a sufficient total time period had been modeled.

The front was established parallel to the y axis, with the perturbations in the x direction as shown in Fig. 2. The model grid was set up with one hundred points in the y direction (with three points overlapping as described in section 2.8), and forty points in the x direction. To specify a location we may use a grid coordinate system based on these points. In this system the x coordinate ranges from

one to forty and the y coordinate ranges from one to one hundred, with the point (1,1) located in the lower left corner. For most of the cases run, the unperturbed portion of the front was initially set at an x position of 3.5 in grid coordinates. For some cases the initial frontal position was set at a larger x value to allow room in the grid for the front to move to the left. This condition arose when the frontal propagation speed was negative.

The testing of the model was performed with a set of parameter values characteristic of the Gulf Stream downstream of its point of separation from the continental margin. The parameter values used for the testing are shown in Table 1.

This choice of parameters determined values for several related variables. These are shown in Table 2.

The disturbance initially imposed on the front had a wavelength of 300 km and an amplitude of 100 km. The cross-stream Froude number was set at -0.02. This value was chosen because preliminary tests indicated that the model was most unstable near the inertial frequency with a negative Froude number, and -0.02 was the largest value that seemed physically reasonable.

Several types of stability must be considered here. The first is the numerical stability of the numerical scheme. An inaccurate numerical scheme can yield incorrect results in the form of a divergent solution ('blow up') which is easily detectable. No errors of this type occurred for any run. A numerical scheme can also give an erroneous

Table 1
Model parameters for the Gulf Stream front

Grid Spacing (x and y)	10 km
Time Step	855.974 s
Stratification ($\Delta\rho/\rho_\infty$)	0.0013
Latitude	39° N
D_b	300 m
D_o	900 m

Table 2
Physical characteristics of the modeled frontal region

Inertial period	19.02 hr
g' (reduced gravity)	0.0127 m/s ²
c (maximum internal wave speed)	3.386 m/s
Maximum internal wave speed at the front	1.955 m/s
λ (baroclinic Rossby radius)	36.9 km

result in the form of a non-convergent solution which is more difficult to detect. The model was checked for non-convergence by testing the dependence of the results on the size of the time step and the grid spacing, as discussed in section 5.3.

The second stability consideration is the response of the model to oscillations near the inertial frequency. Numerical models commonly respond strongly to excitation near 'natural' frequencies, such as the inertial frequency. For example, in a general circulation model investigating baroclinic instability, Orlanski and Cox (1973) observed significant inertial frequency oscillations along the front associated with the Florida Current. If there is no mechanism in the model to dissipate the energy in these oscillations, as there must be in the ocean, they can grow with time and eventually dominate all of the motion in the model. Since the main interest of this investigation involves oscillations at frequencies much lower than inertial, oscillations near the inertial frequency are of secondary importance. To keep the high frequency motions from subordinating the low frequency motions, the high frequency motions must be suppressed. This is done through the use of interfacial friction, as discussed in section 5.2. Ideally, we would wish to restrict the inertial oscillations from unlimited growth without suppressing them entirely.

The third type of stability directly pertains to the frontal perturbations which are the subject of this research. These perturbations are spatially large (tens of km) and temporally slow (several inertial periods). The main question to be asked here is: under what

circumstances are these perturbations unstable? The criteria of stability may be set in two ways. Since the initial amplitude of an applied perturbation is known, the amplitude at a later time may be compared to see if it is increasing (unstable) or decreasing (stable). Alternately, since the initial kinetic and potential energies are known, the ratios of perturbation energy to mean energy can be calculated at a later time to see if they are increasing (unstable) or decreasing (stable).

Imposing the latter two criteria for stability can (and sometimes will) lead to conflicting conclusions. We may relate this conflict by analogy to a surface gravity wave approaching a shore over a bottom with a shallow slope. In that system kinetic energy is lost due to turbulence within the fluid and friction along the bottom. Although these losses are slow, they occur most rapidly where the deviations from the mean are the greatest, i.e. near the wave crest. Meanwhile, the amplitude of the wave increases with time. In the case of a surface gravity wave all of the energy of the system is wave (fluctuation) energy, so that fluctuation to mean energy ratios are not meaningful. However, it can be seen that the total fluctuation energy will decrease over time, indicating stability. At the same time, however, the surface slope and the amplitude of the wave are increasing, indicating instability. Thus, the stability of the interface, exhibited by the amplitude, does not necessarily follow the stability of the interior flow, exhibited by the kinetic energy.

In this study the displacement amplitude criterion is used because it relates to other properties that are computed, e.g., phase speed, and also relates to observable properties. The energy criterion is used to examine the dynamics of the flow and to allow broader conclusions to be drawn regarding the nature of the instabilities.

5.2 - Selection of the Coefficient of Friction

As described above, interfacial friction is used in this model, in part, to stabilize the computations with respect to inertial oscillations. The corresponding coefficient of friction, C_D , cannot be determined readily from observational results. Several values were tried in the model to determine the value best suited for damping the spurious inertial oscillations. Tests were run for friction coefficients of 0.0010, 0.0015, 0.0020, and 0.0040. Plots of the corresponding kinetic energy fluctuations with time are shown in Fig. 6a-d. These plots express the kinetic energy as normalized by the initial kinetic energy E_K/E_{K_i} . The variation in kinetic energy shows that the two smaller values of C_D led eventually to increasing inertial frequency oscillations which led rapidly to velocities in excess of c and thus to termination of the computations, while the largest value showed over-damping. Accordingly, a value of 0.002 was selected for C_D for all of the model runs.

The use of interfacial friction makes the bottom boundary of the model (the interface) a net sink of kinetic energy. Although some energy can be introduced into the model at the parent pool boundary in

the form of potential energy, this was not enough in these tests to compensate for the energy loss. The percentage losses of kinetic and potential energy as a function of C_D are shown in Fig. 7. The x axis intercepts indicate that at a small C_D the net losses would vanish. However, a value of C_D that small would not have been effective in suppressing the inertial oscillations.

Net losses of both kinetic and potential energy were seen for all cases. The differences in the rates of loss between cases was not caused primarily by differences in the evolution of the frontal perturbations. Therefore, the absolute magnitudes of the energies were not used for comparison. Instead, ratios of the fluctuation to mean energies (as determined by Eq. 2.6.3-2.6.6) were used to compare the stability characteristics. It should be noted that the fluctuations measured thus are with respect to means taken in the y direction.

5.3 - Sensitivity Tests

As stated above, the standard time step and grid spacing were set at 855.974 seconds and 10. km, respectively. To ensure that the results of the model were convergent and not sensitive to the choice of either of these, test runs were made with different values for these parameters. The maximum time step allowed for numerical stability is fixed by the grid size and the speed of the fastest internal wave. The ratio of the time step used to this maximum time step is the Courant number, and must be less than or equal to one. For the

standard case the Courant number is 0.82. To test the time step sensitivity a run was made with a Courant number of 0.65, or a time step of 570.649 seconds. For the grid spacing sensitivity test an 8 km grid was used. The Courant number for this latter test was set at 0.82, as in the standard case, so the time step was then 684.9 seconds.

The three cases, one standard and two comparison tests, were run for ten inertial periods. This required 800 time steps for the standard case, 1000 for the grid sensitivity test, and 1200 for the time step sensitivity test. Contours of depth at the initial time and, for each test case, after ten inertial periods are shown in plan view in Fig. 8. The major features of these three figures are quite similar, although there are small differences. The two cases with the higher Courant number have a greater amount of short wavelength variation in the deep region as shown by the oscillations of the 0.9 contour line. Along the leading side of the disturbance the low Courant number case appears to be slightly more rounded. Minor variations are also seen elsewhere along the front.

Other physical properties of the results were computed for intercomparison. The phase speed was determined by following the movement of the point of maximum disturbance. The position of this point was determined from a least squares fit of a cubic of the five points with the largest x coordinate values. The phase speed was computed from a linear least squares fit of a series of these points sampled every half inertial period. Positive values mean that the

wave is moving towards the top (downstream) of the grid. The frontal propagation speed was taken as the speed in the x direction of the straight, unperturbed portion of the front near the top and bottom boundaries. Positive values mean that the front is moving towards the right (parent pool). The amplitude was calculated as the difference in x position between the point of maximum disturbance (crest) and a point determined similarly as the smallest x position point along the front (trough). These results are compared in Table 3.

These figures are quite close, generally within 2%, and indicate that the dependence of the model on the differencing parameters is slight. The grid sensitivity test showed the greatest variation, indicating that greater spatial resolution would be a more important improvement than a decreased Courant number. Greater resolution would also suppress the short wavelength variations shown in Figs. 6b) and c).

The ratios of fluctuation energy to mean energy were computed for both the kinetic and potential energies. The initial and final (after ten inertial periods) values of these ratios for the three test cases are shown in Table 4.

The results for the standard and the time sensitivity cases were again quite close, within 4%. The values of the ratios for the grid sensitivity test were uniformly higher than the corresponding values for the other two cases since the grid sensitivity test used the same number of grid cells as the other tests but a smaller grid

Table 3
Disturbance propagation results for sensitivity tests

	Standard	Time Sensitivity	Grid Sensitivity
Phase speed (cm/sec)	3.94	3.96	3.89
Frontal speed (cm/sec)	2.42	2.37	2.37
Amplitude (km)	108.3	106.8	106.5

Table 4
Fluctuation to mean energy ratios for sensitivity tests

	Standard	Time Sensitivity	Grid Sensitivity
Kinetic ($\times 10^{-3}$)			
Initial	119.	119.	147.
Final	336.	351.	443.
% Increase	282.	295.	301.
Potential ($\times 10^{-4}$)			
Initial	29.2	29.2	32.3
Final	53.1	51.7	65.9
% Increase	182.	177.	204.

spacing, the total horizontal span of the model was reduced. The reduced span caused the applied perturbation to occupy a larger fraction of the model grid. Therefore, the perturbation components of the energies were a larger fraction of the total energies. Proportionally, the differences between the initial and final ratios for the grid sensitivity case were quite similar to the ratios for the other two cases.

These sensitivity tests demonstrate that the model is numerically convergent. The set of differencing parameters used is acceptable and the results were not seriously affected by the choice of either the Courant number or the grid spacing. Thus, for the model runs intended to approximate the conditions of the Gulf Stream the Table 1 values were used.

MODEL RESULTS

6.1 - Introduction

With the model verified as numerically convergent and with the growth of the high frequency motions controlled by friction, the effect of variations in the free parameters on the stability of the flow may be examined. In these tests conditions characteristic of two regions where persistent fronts occur were used. The regions were the Gulf Stream downstream of its point of separation from the continental margin, and the Sargasso Sea at 30° N. These regions were defined by the latitude, parent pool depth, inner/outer boundary depth and stratification. These regions were chosen to represent two different oceanographic regimes. The Gulf Stream is a swift, deep current which is the predominant dynamic feature in its region. The currents connected with the Sargasso Sea fronts are much slower and shallower. They appear to have a seasonal existence as opposed to the permanence of the Gulf Stream (Voorhis, 1969). They are, however, sufficiently long lived (several months) to qualify as permanent for the purposes of this discussion.

In modelling fronts in these two regions several other parameters were expected to influence the flow. For both regions the cross stream Froude number and the amplitude of the initial disturbance

were varied to determine the effect on the propagation of the disturbance. For the Sargasso Sea front the wavelength of the initial disturbance was also varied.

6.2 - Gulf Stream Unperturbed Front

Before testing the stability characteristics of a perturbed front, the general characteristics of an unperturbed (straight) front were examined. The characteristics of greatest interest were the frontal cross stream propagation speed and the change in the kinetic and potential energies with time. Trials were made for three cases with varying cross stream Froude numbers, $F_r = -0.02$, $F_r = 0.00$, $F_r = 0.01$. The $F_r = 0.00$ value was chosen to provide a test with no induced cross flow so that the 'basic' dynamics could be studied. A Froude number with a magnitude of 0.02 was considered the largest that was physically realistic. Both positive and negative Froude numbers were used to test the effect of the direction of the cross stream flow, but a value of 0.02 yielded a frontal propagation speed that was too large to be plausible (see below). Accordingly, the positive Froude number was reduced to 0.01, while the negative remained at -0.02.

For each of the three Froude number cases the model was run for ten inertial periods. The trials with $F_r = -0.02$ and $F_r = 0.00$ were started with the front at an x position of 3.5 grid coordinates. The trial with $F_r = 0.01$ was run with the front initially at an x position of 5.5 grid coordinates. To test the (possible) effects of the model boundaries on the frontal movement an extra run was made for $F_r = 0.01$,

started with the front at an x position of 3.5 grid coordinates. This test was run for four inertial periods. The left boundary cannot affect the results of this model as long as the front is at least one grid cell away from it. The right (parent pool) boundary might affect the flow if it is not a sufficiently large distance from the front. A significant difference between the two $F_r = 0.01$ cases would indicate an insufficiently large model domain. The position of the front as a function of time for each of these four cases is plotted with open symbols in Fig. 9. The four lines with solid symbols at the end points are least squares linear fits to the frontal positions, taken once per inertial period.

For the negative Froude number case the front moved toward the right (larger x values). For the other two cases the motion was to the left (smaller x values). For all of the cases the motion of the front was nearly uniform throughout the run. Frontal propagation speeds were calculated from the least squares fits and are shown in Table 5. This table also includes the results of a test with $F_r = -0.02$ for which the initial position of the front was along $x = 12.5$ grid coordinates.

The difference in initial position for the $F_r = 0.01$ cases had a negligible effect on the frontal propagation speeds. The greater difference in starting position between the two $F_r = -0.02$ cases affected the speed less than 3%. This result indicates that the model domain is large enough in the x direction so that the presence of the parent pool boundary does not significantly affect the motion of the free boundary.

Table 5
Frontal propagation speeds for an unperturbed front

Froude number	Initial position	Speed (cm/s)
-0.02	3.5	2.41
-0.02	12.5	2.34
0.00	3.5	-2.48
0.01	3.5	-4.94
0.01	5.5	-4.98

Thus, the initial x position was set at 3.5 for the tests in which the front moved to the right. For those tests in which the front moved to the left, the initial x position was set at a sufficiently large value to keep the front in the grid for the entire test.

The zero Froude number case indicates that the flow was not exactly in geostrophic balance. The deviation from geostrophy was probably caused in part by the interfacial friction which slightly reduced the downstream velocity. If the downstream velocity is not sufficient to geostrophically balance the pressure gradient from the slope of the interfacial depth, a compensating cross stream flow will develop. Such a cross stream flow was observed and was influenced by the Froude number, as shown in Fig. 10. The velocities shown in Fig. 10 are relative to the front, which is moving, rather than to the fixed grid.

The results in Table 5 show that the presence of basic state across frontal flow (non-zero Froude number) affects the propagation of the front across the grid. The changes in the cross stream frontal propagation speed are only a few percent of the downstream velocity, which indicates that they are second order. The mechanisms causing these changes from the zero Froude number case are not clear, but were probably connected with the variations in the relative cross stream velocity shown in Fig. 10. Although all of the cases showed positive relative cross stream velocities and volume losses, the negative Froude number case (dashed line) had smaller velocities than either the $F_r = 0.00$ or $F_r = 0.01$ (dotted line) cases. In spite of a loss in

volume and a positive relative cross stream velocity, the $F_r = -0.02$ case showed a rightward movement in the front.

The series of frontal positions shown in Fig. 9 shows that the flow supporting the cross frontal propagation of the front developed rapidly and continued uniformly through time. In the range of F_r examined this effect was linear; that is, the change in the frontal propagation speed was proportional to the cross stream Froude number, approximately 2.5 cm/s for each 0.01 increment in the Froude number. Since the frontal propagations for the zero and negative Froude number cases were in opposite directions, a negative Froude number may be necessary for the front to maintain a fixed position on the grid over a long period of time. These results suggest a value of -0.01 for the Froude number. Kao (1980) obtained an equilibrium state for the Gulf Stream with a cross flow of approximately the same magnitude. The cross stream flow was required for the maintenance of the frontal volume. He suggested that an alongfront pressure gradient (which could not be used here due to the periodic boundary conditions) would serve to hold the front stationary.

Another important result was the change in the kinetic and potential energies with time. These were calculated from the model results using (2.6.3)-(2.6.4) at the initial and final (after ten inertial periods) time steps. As shown in Fig. 10 the downstream velocity, and hence the kinetic energy, is greatest near the front and diminishes to a negligible value at the parent pool. The depth, hence the volume and potential energy, is smallest near the front and rises

to a near constant value towards the parent pool. All three cases showed some flattening of the interface and thus some loss of volume in the frontal region. Kinetic energy losses occurred in all cases due to the influence of interfacial friction, as discussed in section 5.2. The losses for these tests were within 3% of each other. Small losses also occurred in the potential energies consistent with the decreases in volume. Slight variation between the tests occurred. The $F_r = -0.02$ test showed the least volume decrease and the $F_r = 0.01$ test showed the most.

6.3 - Gulf Stream Small Amplitude Perturbation

To study the behavior of perturbations on the Gulf Stream front, tests were run with two values for the amplitude to wavelength ratio for the initial disturbance. The first set of tests had a small amplitude to wavelength ratio of 0.0333, with an amplitude of 10 km and a wavelength of 300 km. These tests were run with the same set of cross stream Froude numbers that were used in the unperturbed front cases. They were run for only six inertial periods due to the development of occluding instabilities along the front, as will be discussed later.

The perturbations initially applied to the free boundary were centered lengthwise along the front. Thus, portions of the front at the top and bottom edges of the model grid were initially straight and undisturbed by the frontal perturbation. This was done to eliminate edge effects near the perturbation and to allow room for movement of

the disturbance along the front. These unperturbed portions of the front were also used to measure the frontal propagation speed in the cross frontal direction for comparison with the unperturbed front results. Table 6 shows the initial x positions of the front in grid coordinates and the resulting frontal propagation speeds.

Different initial positions were used to allow room for the leftward propagating fronts. These results agree very well with those in Table 5. This indicates that the dynamics of the regions well away from the perturbation are not affected by a perturbation of this scale.

Time sequences of the frontal position are shown in Fig. 11 a-c) for $F_r = -0.02$, 0.00 , and 0.01 , respectively. Since the perturbation is very small, the x coordinate in all cases has been expanded by a factor of five. The time sequence starts with the leftmost curve of each figure. The frontal position is displayed once per inertial period thereafter. These curves show similar patterns of deformations at the back of the bulge (toward the bottom side in the figure) evolving into short, steep disturbances which propagate very rapidly to the leading side of the bulge. This tendency was very mild for $F_r = -0.02$ compared with the other two cases. Small disturbances also formed downstream of the bulge. In two cases ($F_r = -0.02$ and 0.00) these grew rapidly and 'occluded' (several free boundary drift points crossed so that the free boundary formed a closed loop) shortly after six inertial periods. This condition caused computational difficulties and forced termination of the runs.

Table 6

Frontal propagation speeds for 10 km initial disturbance

Froude Number	Initial Position	Speed (cm/s)
-0.02	5.5	2.52
0.00	7.5	-2.48
0.01	7.5	-5.03

The bulges associated with the initial disturbance moved and amplified over this time span. The phase speeds and amplitudes were measured by the same method that was discussed in chapter 5. In linear models amplitude growth rates have an exponential time dependence which appears as an imaginary component of the disturbance phase velocity (Orlanski, 1969). We assume such a simple relation:

$$A = A_0 \exp(gt) \quad (6.3.1)$$

where t is the time, A_0 is the initial amplitude, A is the amplitude at time t and g is the growth rate. The formula for the doubling time derived from this is:

$$T_2 = \ln(2)/g \quad (6.3.2)$$

where T_2 is the doubling time. The results of these calculations are shown in Table 7.

The effects of the short wavelength disturbances were excluded from the amplitude calculations readily by a curve fitting procedure. It was not possible, however, to entirely exclude these effects from the phase speed calculations. This may partially explain the lack of a simple pattern in the phase speed results, such as was seen for the frontal propagation results in Tables 5 and 6. The results are, however, in reasonable agreement with the observationally determined values of 4 to 8 cm/s. The doubling times agree roughly with the results of other models (e.g. Orlanski, 1969; Lipps, 1963; Tareev, 1965). These models were linear, small amplitude models. The observational results of

Table 7
Results for 10 km initial disturbance

Froude Number	Phase Speed (cm/s)	Final Amplitude (km)	Doubling Time (Inertial Periods)
-0.02	7.18	18.0	7.08
0.00	11.32	13.1	15.40
0.01	3.60	13.5	13.86

Hansen (1970) indicate that these times are much too short. However, the observational results were based primarily on larger amplitude disturbances. As will be seen in section 6.4, the amplitude of the disturbance can have a profound effect on the growth rate.

The negative Froude number case showed the greatest tendency toward instability according to the frontal displacement amplitude criterion defined in chapter 5. The growth of the main disturbance was much faster and the smaller disturbances began earlier and were more numerous. The $F_r = 0.01$ case was the least unstable in this respect. The relative stabilities from the energy calculations may be used for comparison. The mean and fluctuation components of the kinetic and potential energies were calculated from (2.6.3)-(2.6.6). The ratios of fluctuation to mean energies are shown in Table 8 for the initial and final (after ten inertial periods) values.

These results showed interesting differences from those in Table 7. The $F_r = 0.01$ case showed the greatest increase in fluctuation kinetic energy and the $F_r = -0.02$ case had the smallest increase. This would imply that the $F_r = 0.01$ case was the most unstable. The potential energy ratios also show a different pattern from the frontal displacement amplitude changes, with $F_r = 0.01$ the most unstable and $F_r = -0.02$ the least. The $F_r = 0.01$ case had a loss of total potential energy while the other two increased. The $F_r = -0.02$ case had the smallest loss of total kinetic energy and the $F_r = 0.01$ case had the greatest.

Table 8

Fluctuation and mean energy for 10 km initial disturbance

	-0.02	0.00	Froude Number 0.01
Kinetic			
Initial			
Mean	45.96	42.18	42.91
Fluctuation	0.2408	0.2415	0.2800
Ratio ($\times 10^{-3}$)	5.24	5.72	6.53
Final			
Mean	37.82	33.39	36.56
Fluctuation	0.8927	1.1413	2.5395
Ratio ($\times 10^{-3}$)	23.6	34.2	69.5
Potential			
Initial			
Mean	2893.	3007.	3201.
Fluctuation	0.4029	0.4091	0.4177
Ratio ($\times 10^{-4}$)	1.39	1.36	1.31
Final			
Mean	2940.	3026.	3188.
Fluctuation	0.8040	1.1019	2.0060
Ratio ($\times 10^{-4}$)	2.73	3.64	6.29

For small amplitude meanders the cross stream flow has a significant effect on the behavior of the free boundary and on the energy flow in the outer region. Although the doubling times are short compared to observational results, they are in general agreement with other small amplitude model results. The negative Froude number case appears to be the most unstable in frontal amplitude, but the most stable in the outer region flow. It also matched most closely the observed phase speed and had the most rapid amplitude growth. The two stability criteria are clearly related to different aspects of the flow, since the results for the two are opposite.

6.4 - Gulf Stream Large Amplitude Perturbations

The second group of tests which were run for the Gulf Stream front had a large amplitude to wavelength ratio with a value of 0.333. The initial disturbance for these cases had wavelengths of 300 km, as in the small amplitude perturbation tests, but had an amplitude of 100 km. The same set of cross stream Froude numbers, -0.02, 0.00, and 0.01 was used. All of the cases were run to ten inertial periods and the $F_r = -0.02$ case was extended to thirty four inertial periods, as a test of the long term behavior of the model. An additional case with $F_r = -0.02$ and an inverse bulge was also run. The inverse bulge was a perturbation which extended the front to the left instead of to the right as in the other cases.

The frontal propagation speeds were calculated in the manner described in section 6.3, and are shown in Table 9. The inverse bulge

Table 9
Frontal propagation speed for 100 km initial disturbance

Froude Number	Initial Position	Speed (cm/s)
-0.02	3.5	2.42
-0.021	12.5	2.41
0.00	5.5	-1.76
0.01	7.5	-4.57

case has a Froude number designation -0.02I to distinguish it from the 'normal' case with $F_r = -0.02$.

The two negative Froude number cases show excellent agreement with each other and with the results in Tables 5 and 6. The zero Froude number case shows a significant reduction in magnitude from the previously observed values. The $F_r = 0.01$ speed is also smaller in magnitude than was seen earlier.

Frontal position and depth contours after ten inertial periods are shown in Fig. 12a-d). Since the flow is primarily geostrophic, the movement of the water is nearly along the depth contours. These contours therefore approximate streamlines. The contours are much closer together in Fig. 12a) than in b) or c). This indicates that the downstream velocities are highest for $F_r = -0.02$. The fluctuations in the deepest contours near the bottom of each figure are the result of waves propagating along the interface. The $F_r = -0.02$ case appears to be much less affected by these than the other two cases. In all of the figures the contours are closer together on the upstream side of the main bulge (towards the bottom of the figure) than on the downstream side. This indicates increased velocities on the upstream side. The increased momentum seems to have carried the water farther away from the unperturbed frontal position as it flowed around the main bulge. The points of maximum deflection are progressively farther downstream for the deeper contours. The deepest contour for $F_r = -0.02$ appears to have the greatest angle relative to the unperturbed frontal position and its maximum deflection point is carried further downstream than in

the other two cases. In all three cases the deepest contour showed approximately the same amount of deflection as the front. Thus, the cross stream flow is seen to affect the downstream velocity and the direction of the flow across the entire frontal region. The inverse bulge case shown in Fig. 12d) was the only one in which the initial disturbance did not amplify. In that case the contours show the most crowding on the downstream side of the main bulge. The deepest contour showed almost no deflection.

Time sequences of the frontal position are shown in Fig. 13a-d) for $F_r = -0.02, 0.00, 0.01$, and $-0.02I$. The sequences start with the initial curve at the left. Subsequent frontal positions are shown at two, six, and ten inertial periods. All of these cases show an initial steepening at the forward side of the bulge. In the $F_r = -0.02$ case the steepening abated later in the run and the bulge became rounder. In the other three cases the steepening continued, particularly in the $F_r = 0.01$ and $-0.02I$ cases.

In each case a complementary bulge (opposite in direction from the original bulge) formed in front (downstream) of the original disturbance. These complementary bulges, in turn, had complementary bulges form in front of them. Simmons and Haskins (1979) also observed the development of disturbances downstream of an initial perturbation. In their experiment the downstream disturbances grew to a size equivalent to the evolved size of the initial perturbation. The movements of the complementary bulges suggest group velocities much greater than the phase velocities of the perturbations. If we regard these distur-

bances as dispersive components of the flow, the associated group velocities would be 80 cm/s for $F_r = -0.02$, 66 cm/s for $F_r = 0.00$, and 58 cm/s for $F_r = 0.01$. The complementary bulges developed weakly for $F_r = -0.02I$, but suggest a group velocity equal to the $F_r = -0.02$ case. These figures agree with the (widely scattered) group velocities in the models reviewed by Hansen (1970) which ranged from 11 to 100 cm/s.

The main disturbance wavelengths in all cases tended to grow. This effect was most pronounced in the $F_r = -0.02$ test. Two explanations are possible. One assumes that these disturbances are dispersive, and the other assumes that they are separable into spatially and temporally growing components.

The initially imposed disturbance has the form $F(y) = B(0)[\cos(\pi y) + 0.5]$, where $B(0)$ is a boxcar function (square wave) one wavelength wide and centered at zero. The spatial Fourier transform of this is $F(k) = 0.5[\text{sinc}(1-k) + \text{sinc}(1+k) + \text{sinc}(k)]$, where k is the alongfront wave number and $\text{sinc}(s) = \sin(\pi s)/\pi s$. The initial disturbance is thus harmonically rich. If these waves were dispersive, then as the various components begin to separate, the disturbed region, and hence the apparent wavelength, would grow. For the Froude number to affect the rate of increase of the wavelength, it would have to affect the dispersive character of the perturbations.

The increase in wavelength does not, however, require dispersive behavior. As suggested by Thacker (1976), the disturbance may be separable into spatially and temporally growing components (see for

example his eq. 18). A wave which has both spatially and temporally growing components would show an increase in apparent wavelength as the two components separated in space. To affect the rate of the apparent increase of the wavelength, the Froude number would have to affect the growth rates of the two components and/or the propagation rate of the spatially growing component.

The shapes of the bulges in Fig. 13 are also indicative of the nature of their propagation. The trailing sides of the bulges tended to become smoother and flatter with time. Although the locations of the rearmost parts of the perturbations became difficult to distinguish precisely, they generally retained their positions or advanced slightly. The forward sides and the amplifying portions of the perturbations clearly moved forward. This supports the hypothesis that the disturbances are both spatially and temporally growing.

The amplitudes, phase speeds and doubling times were computed in the same manner as in section 6.3. These are shown in Table 10.

All of the tests showed amplification except the inverse bulge. The flow in the outer region was apparently unable to continue to supply energy to this perturbation. The disturbance amplitudes did not show a temporally uniform growth in any of these tests. The results in Table 10 must then be regarded as having significant possible errors, so that there may be little real difference in the actual doubling times. This would imply that the cross stream flow does not have a major effect

Table 10
Results for 100 km initial disturbance

Froude Number	Phase Speed (cm/s)	Final Amplitude (km)	Doubling Time (Inertial Periods)
-0.02	3.94	108.3	86.9
-0.021	3.64	93.0	-
0.00	2.94	107.2	99.7
0.01	2.54	110.0	72.7

on the growth rates for large amplitude perturbations, while it does for small amplitude disturbances.

The doubling times seen here are much longer than those seen for the small amplitude disturbances (the amplification rates are lower) and are much closer to the observationally determined values. As noted above, the observational results were obtained for finite amplitude meanders. Thus, the tests for the large amplitude disturbance were more nearly representative of the observational conditions than were the small amplitude tests. These results indicate that the nonlinear effects in finite amplitude disturbances significantly reduce the growth rate. In the model of Orlanski and Cox (1973), the growth rate for the finite amplitude disturbances was an order of magnitude lower than that for the linear (small amplitude) models. The small amplitude growth rates measured here were $0.5 \times 10^{-6} \text{ s}^{-1}$ to $1.1 \times 10^{-6} \text{ s}^{-1}$ versus the $0.96 \times 10^{-6} \text{ s}^{-1}$ to $1.2 \times 10^{-6} \text{ s}^{-1}$ rates seen by Orlanski and Cox. The finite amplitude disturbance rates were $0.081 \times 10^{-6} \text{ s}^{-1}$ to $0.093 \times 10^{-6} \text{ s}^{-1}$ here versus $0.085 \times 10^{-6} \text{ s}^{-1}$ to $0.22 \times 10^{-6} \text{ s}^{-1}$, showing very good agreement between the two models. Simmons and Hoskins (1978, 1979) and Pedlosky (1979) also found a severe reduction in growth rates as the instability amplitude increased.

The phase speeds were also lower here than for the small amplitude disturbances. These speeds are slightly lower than the 4 to 8 cm/s speeds obtained from observations. A trend of increasing speed with decreasing Froude number can be identified.

The character of the energy changes also differed significantly from that in the small amplitude tests. The fluctuation to mean component ratios are shown in Table 11.

The inverse bulge case showed a decrease in both the fluctuation components, which is consistent with the reduction in the amplitude of the disturbance which was observed in Table 10. The other three tests showed increases in the ratios. Although not directly comparable, the increases were smaller than those seen in Table 8 for the small amplitude disturbances. This also indicates that the amplification processes are slower for the large amplitude perturbations. The differences seen between the three Froude number tests were small. This agrees with the results of the growth rate calculations showing that the effect of the Froude number was greatly reduced for these tests.

To determine the long term behavior of the model, the test with $F_r = -0.02$ was continued for a total time of thirty four inertial periods. During this time the frontal disturbance continued to advance and amplify. Depth contours are shown in Fig. 14 at eighteen and thirty four inertial periods. The general pattern shown in Fig. 12 is continued, with the wavelength increasing, the original bulge becoming less steep and the complementary bulge in front of it becoming deeper and more steep. Due to the periodic boundary conditions and the relatively high group velocity, the disturbances which were advancing ahead of the main perturbation had crossed the top boundary, reentering the grid at the bottom boundary and had caught up to the trailing (bottom) side by the end of thirty four inertial periods. At this point they were beginning

Table 11
 Fluctuation to mean energy ratios for 100 km
 initial disturbance amplitude

	-0.02	Froude Number -0.02I	0.00	0.01
Kinetic ($\times 10^{-3}$)				
Initial	119.	213.	125.	124.
Final	158.	186.	215.	274.
Potential ($\times 10^{-4}$)				
Initial	29.2	60.9	28.8	28.9
Final	42.2	22.1	64.3	70.2

to affect the behavior of the main perturbation, so the test was terminated.

The propagation of the front across the grid continued steadily, with the frontal propagation speed varying less than 5% from the value given in Table 10. The evolution of the perturbation also continued at approximately the same rate as for the first ten inertial periods. The results of the phase speed and amplification calculations are shown in Table 12.

As noted above, the increase of the disturbance amplitude was not uniform in time, thus creating the differences in the doubling times. These results are, however, reasonably close to each other and still show a marked increase from the small amplitude case. As the wavelength of the main bulge increased, the kinetic energy fluctuation to mean ratio showed non-uniform behavior. The fluctuation to mean kinetic energy ratio rose from 158×10^{-3} at ten inertial periods to 218×10^{-3} at eighteen inertial periods. It then declined to 178×10^{-3} at thirty four inertial periods. This may have been a result of the inertial period oscillations. The kinetic energy in the inertial period oscillations increased with time as shown in Fig. 15. The oscillations which were initially small began increasing significantly after about fourteen inertial periods. Orlanski and Cox (1973) observed a similar increase in near inertial oscillations in their model. In that study the inertial period waves were shown to be caused by baroclinic instability.

Table 12
Results for extended run of 100 km initial disturbance

Time (Inertial Periods)	Phase Speed (cm/s)	Final Amplitude (km)	Doubling Time (Inertial Periods)
18	2.64	120.1	68.12
34	2.91	131.0	86.54

Spectra were calculated for the data shown in Fig. 15 for the time intervals 0-14 and 14-34 inertial periods, and are shown in Fig. 16. The error bars show the 90% confidence intervals. After fourteen inertial periods the energy in the inertial frequency band (and its harmonics) greatly increases. The low frequency peak in 16a) is missing entirely in 16b). In general, the earlier segment showed lower variance, as expected from Fig. 15. The slope at the higher frequencies is approximately $-1/3$. Processes involving turbulence usually exhibit a $-5/3$ slope. This behavior is consistent with the model operating in an inviscid manner, as initially intended.

6.5 - Sargasso Sea Short Wavelength Perturbation

Persistent oceanic fronts have been observed in the Sargasso Sea (Voorhis and Hersey, 1964; Voorhis, 1969; Katz, 1969). A set of oceanographic conditions characteristic of this region were used to define the second frontal regime considered in this investigation. The parameters used in the model are listed in Table 13.

These fronts are much shallower than the Gulf Stream front, and are also narrower (smaller Rossby radius). The maximum internal wave speed is lower and the inertial period is longer, implying that the frontal processes will be slower.

Observations of the surface thermal field (e.g. Voorhis, 1969) indicate the presence of a range of perturbation wavelengths. Since the wavelength of a disturbance may affect its stability characteristics,

Table 13
Model parameters for Sargasso Sea front

Stratification ($\Delta\rho/\rho_\infty$)	0.0013
Latitude	30° N
D_b	50 m
D_o	200 m
Inertial Period	23.94 hr
g' (reduced gravity)	0.0127 m/s ²
c (maximum internal wave speed)	1.596 m/s
Maximum internal wave speed at the front	0.798 m/s
λ (baroclinic Rossby radius)	21.9 km

tests were performed with two initial disturbance wavelengths. These were chosen as 30 km and 100 km to cover the observed range. All of the tests were run for ten inertial periods.

For the short wavelength tests a grid spacing of 2 km and a time step of 359.129 s were used. This results in a Courant number of 0.81, which is very close to the 0.82 value used previously. A small initial amplitude of 3 km was used. To determine the dependence of the frontal evolution on the cross stream flow, the same set of Froude numbers that was used in the previous tests was also used here. The frontal propagation speeds were calculated as before and are shown in Table 14.

As seen previously, the Froude number is a major determinant of the propagation speed. The speeds seen here are much smaller than those for the Gulf Stream front, consistent with the expectation of generally slower movement. The speed variation was approximately 0.5 cm/s for a 0.01 increment in F_r .

Time sequences of the frontal position at one inertial period intervals are shown in Fig. 17a-c) for $F_r = -0.02$, 0.00, and 0.01, respectively. The x coordinate has been expanded by a factor of five in all cases. The evolution of these disturbances was initially similar to the evolution of the Gulf Stream front disturbances. An initial steepening of the leading edge and the formation of a complementary bulge occurred for all cases. However, for the $F_r = 0.00$ and 0.01 cases the complementary bulge rapidly diminished in amplitude and was an

Table 14
Frontal propagation speeds for 30 km
wavelength initial disturbance

Froude Number	Initial Position	Speed (cm/s)
-0.02	5.5	0.13
0.00	5.5	-0.83
0.01	9.5	-1.36

indistinct feature within five inertial periods. Because of this rapid diminution, meaningful group velocities could not be calculated. For the $F_r = -0.02$ case the complementary bulge was maintained longer, but eventually vanished also. Based on the motion during the first eight inertial periods the group velocity was 8.08 cm/s for this case. This is much lower than the group velocities seen in the Gulf Stream large amplitude tests. The $F_r = 0.01$ case developed short wavelength disturbances, similar to those seen in the Gulf Stream small amplitude tests, although here they did not grow to occlusion. The phase speeds and final amplitudes are shown in Table 15.

The two non-zero Froude number cases had similar phase speeds, while the phase speed for the $F_r = 0.00$ case was somewhat lower. Although there are no reliable observational data for comparison, these results seem to be in a reasonable range. They are generally smaller than the speeds for the Gulf Stream small amplitude tests. The Froude number does not seem to have a major effect on these speeds.

All of the disturbances showed a decrease in amplitude. Considering that the losses of total energy were greater here than for the Gulf Stream front, it appears that these runs may have been overdamped by interfacial friction. The same value of C_D was used here as for the Gulf Stream front. However, since this flow was shallower and slower, a lower value may have been more appropriate. In spite of this, a trend in the results is clear. The $F_r = -0.02$ case maintained a disturbance closest to the original amplitude. The amplitudes of the other two tests decreased steadily to about 60% of the initial value.

Table 15
Results for 30 km wavelength initial disturbance

Froude Number	Phase Speed (cm/s)	Final Amplitude (km)
-0.02	4.69	1.98
0.00	3.62	1.20
0.01	4.59	1.12

This indicates the greatest tendency towards stability in the positive Froude number case, as was seen above, when using the amplitude stability criterion.

The changes in the fluctuation to mean energy ratios were also similar to those of the previous tests. These are shown in Table 16.

These results again indicate that the negative Froude number case has the most stable flow in the outer region and the most unstable disturbance amplitude.

6.6 - Sargasso Sea Long Wavelength Perturbation

As mentioned above, a set of tests were run for the Sargasso Sea front with an initial perturbation wavelength of 100 km. For these tests the grid spacing was 4 km and the time step was 718.258 s, which again results in a Courant number of 0.81. Since the Froude number dependence had been closely investigated previously, a single value of 0.00 was used for these tests. Two model runs were made with initial amplitudes of 3 and 30 km. The amplitude to wavelength ratios were then 0.03 and 0.30, respectively. The frontal propagation speeds are shown in Table 17.

These speeds are significantly higher than those for the short wavelength case. This and the large difference between these two cases indicate a sensitivity to the wavelength of the perturbation.

Table 16
 Fluctuation to mean energy ratios for 30 km wavelength
 initial disturbance

	Froude Number		
	-0.02	0.00	0.01
Kinetic ($\times 10^{-3}$)			
Initial	.404	.319	.401
Final	1.16	8.17	9.78
Potential ($\times 10^{-4}$)			
Initial	.170	.178	.165
Final	.586	3.23	6.09

Table 17
Frontal propagation speeds for 100 km wavelength
initial disturbance

Initial Amplitude (km)	Initial Position	Speed (cm/s)
3	7.5	-1.95
30	7.5	-1.51

A time sequence of the frontal position for the small amplitude case is shown in Fig. 17. The x coordinate has been expanded by a factor of five. The time sequence for the large amplitude case is shown in Fig. 19. The x coordinate is not expanded in that figure.

The leading edge of the small amplitude disturbance followed the general pattern of initial steepening, formation of a complementary bulge, and then a period of decreasing steepness at the leading edge and a deepening of the complementary bulge. In that respect this perturbation behaved more like the Gulf Stream cases than the Sargasso Sea short wavelength case where the complementary bulge did not remain a permanent feature. The trailing edge was anomalously active, initially advancing, then retreating, and then advancing again. During the retreating phases it moved upstream, became very steep, and eventually collapsed. This type of motion was not seen along the Gulf Stream front in sections 6.3 and 6.4. If this process actually occurs in the Sargasso Sea, the meander evolution would be more complex, making accurate observation of phase speeds and growth rates more difficult.

The large amplitude perturbation (Fig. 19) followed the general pattern seen in the Gulf Stream cases. This test also appeared to show the overdamping mentioned above. In addition to the lack of disturbance amplification there was significantly less activity along the interface. Fig. 20 shows interfacial depth contours at the initial and final stages. Although the general pattern is similar to that in Fig. 12b), the very short wavelength fluctuations along the deeper contours are much smaller in Fig. 20b).

The group and phase speeds and the doubling time results are shown in Table 18.

The phase speeds were lower than for the short wavelength case and the group speeds were higher than the value found for $F_r = -0.02$. Although the effects of the possible overdamping are not clear, these tests clearly show greater disturbance amplification tendencies. The short wavelength, zero Froude number test showed significant diminution, whereas these tests showed neutral stability for the 30 km case and amplification for the 3 km case. The 3 km case had a doubling time comparable to the Gulf Stream small amplitude case.

The phase and group speeds showed that the small amplitude case had more rapid movement than the large amplitude case, as was seen for the Gulf Stream. The amplification rates agreed with the prior results in showing greater amplitude instability. The fluctuation to mean energy ratios shown in Table 19 also reflect that pattern.

The growth of fluctuation kinetic energy was slower for the large amplitude test, as was seen before in the Gulf Stream. The decrease in the potential energy ratio for the large amplitude case suggests a straightening of the interfacial depth contours, which is supported by Fig. 19. Comparing the 3 km amplitude case here with the short wavelength test discussed above shows that the growth in the kinetic energy ratio for the long wavelength case was much smaller than that for the short wavelength case while the disturbance amplitude growth was larger. This is the same pattern as was seen above.

Table 18
Results for 100 km wavelength initial disturbance

	Initial Amplitude (km)	
	3	30
Phase speed (cm/s)	2.27	1.89
Group speed (cm/s)	17.4	14.6
Final amplitude (km)	4.60	29.7
Doubling time (Inertial periods)	6.95	-

AD-A115 519

DELAWARE UNIV NEWARK COLL OF MARINE STUDIES
OCEANIC FRONTAL STABILITY: A NUMERICAL MODEL, (U)

F/G 8/10

NOV 81 W W MARTIN

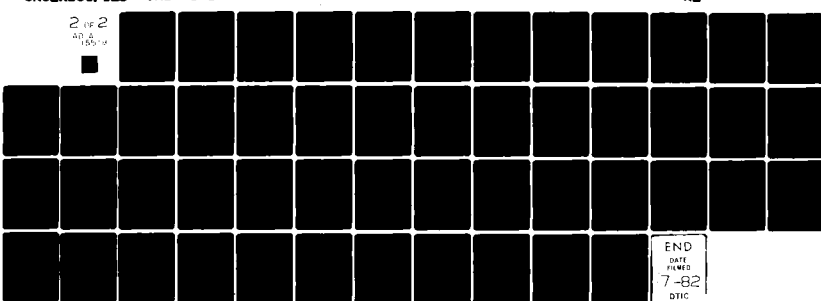
N00014-75-C-0714

UNCLASSIFIED CMS-02-81

ML

2 NF 2

AD A
155-12



END
DATE
FILED
7-82
DTIC

Table 19
Mean to fluctuation energy ratios for 100 km wavelength
initial disturbance

	Initial Amplitude (km)	
	3	30
Kinetic ($\times 10^{-3}$)		
Initial	1.35	54.3
Final	9.33	63.4
Potential ($\times 10^{-4}$)		
Initial	.646	29.0
Final	1.35	23.7

CONCLUSIONS

A stable, convergent model has been developed to study the evolution of mesoscale meanders of oceanic fronts. This model has focused on some of the parameters which affect the stability characteristics of these meanders. Oceanographic conditions representative of two regions, the Gulf Stream downstream of Cape Hatteras and the Sargasso Sea at 30° N, were used to set several of the basic model parameters.

The results of the model were verified where possible by comparison with observations. The only observations available for comparison with the model results are from large amplitude meanders of the Gulf Stream. Both the phase speeds and amplitude doubling times computed from the model results appropriate for these tests were in satisfactory agreement with the observed values.

Since the model employed nearly inviscid dynamics, it should have yielded flows which nearly conserved potential vorticity. Stommel (1976) gave a simple model for the Gulf Stream which assumed geostrophic balance for the alongfront velocity and uniform potential vorticity across the stream. The initial conditions of the present model also used these assumptions, so that the potential vorticity was initially uniform across the model grid. For the tests which ran for ten inertial periods, the potential vorticity field remained uniform to within 3%.

For the extended test, which was run to thirty four inertial periods, the potential vorticity remained uniform to within 7%. This indicates that the model was conserving potential vorticity to within acceptable limits. The small discrepancies are easily accounted for by the slight interfacial friction used for stability. The model potential vorticity field thus provides an independent check on the model results.

Several scalings were used in the development of this model. These were: the baroclinic Rossby radius for length, the inertial period for time, and the maximum internal wave speed for velocity. The model results indicate that the length scale was chosen properly, but that the time and velocity scales were not. The characteristic time scale for the meanders was on the order of many inertial periods, so that the time scaling used was too short and the velocity scaling too large. The velocity scaling was, however, proper for the fluid velocity itself. It is still unclear what the meander time scale should be in terms of flow parameters. Although this model and others with similar scalings yield reasonable results, the lack of a proper time scale indicates that some of the essential physics have yet to be understood. This problem will most likely require further development of theoretical models for its resolution.

Tests were conducted with this model to determine the effects of variation of several model parameters on the evolution of mesoscale meanders. Of those which can affect the behavior of these disturbances,

the wavelength/Rossby radius ratio, amplitude/wavelength ratio, and cross stream Froude number were investigated.

One of the main purposes of the many linear models has been to deduce the wavelength of the fastest growing instability. Nevertheless, in this model, since the predominant wavelength is generally known from observation, it was treated as a given model parameter. In the simple experiment that was performed to investigate the effect of two different wavelengths on stability, significant differences were seen. While the small wavelength/Rossby radius disturbance showed a decrease in amplitude, the large wavelength/Rossby radius ratio disturbance showed significant growth. Furthermore, a large wavelength/Rossby radius ratio disturbance together with a larger wavelength/amplitude ratio also showed an amplitude decrease, but the decrease was not as large as for the short wavelength case. For the Sargasso Sea conditions a 30 km long disturbance was seen to be more stable than a 100 km long disturbance. These results indicate that wavelength/Rossby radius ratio is a significant parameter for this model which affects stability.

The initial amplitude/wavelength ratio was a second parameter shown to have a strong influence on the amplitude growth rate. Several tests were made with amplitude to wavelength ratios from 0.03 to 0.33, using both sets of oceanographic conditions. The small amplitude cases all showed more rapid amplitude growth than the large amplitude cases. For the small amplitude tests using Gulf Stream conditions, the growth

rates were similar to those given by several prior small amplitude analytic models (Lipps, 1963; Tareev, 1965; Orlanski, 1969). The growth rates obtained from the corresponding large amplitude tests closely matched the rates obtained from field and satellite observations, which were primarily of large amplitude disturbances along the Gulf Stream (Hansen, 1970; Halliwell and Mooers, 1979). The amplitude growth rates for the large amplitude disturbances were typically an order of magnitude smaller than those for the small amplitude cases. The non-linear terms in the governing equations likely become a major factor in the finite amplitude dynamics, reducing the amplitude instability as the amplitude increases.

The cross stream Froude number was shown to be a third important parameter for the stability characteristics. The movement of the front in the cross stream direction was related linearly to this parameter. A negative Froude number flow, resulting from downward entrainment in the inner region, was required to eliminate cross stream frontal migration over a long period of time. This downward entrainment also resulted in a decrease in the amplitude doubling time. This decrease was by as much as a factor of two, compared with a case with no cross flow, in the Gulf Stream small amplitude tests.

Two stability criteria were used in these tests. One was based on the amplitude of the disturbance and the other on the fluctuation to mean component ratios for the kinetic and potential energies of the flow in the outer region. These two criteria were shown to be in opposition.

In a given set of tests, the case which was most stable by one criterion was the least stable by the other. This suggests that the flow in the outer region and the deformation of the front were competing for energy from the same source. The energy source most likely was the potential energy in the parent pool, although the energy analysis performed was not adequate to determine this clearly. The transfer of energy was affected by the Froude number, wavelength, and particularly by the amplitude of the disturbance, although these effects could not be quantified. An important extension of this model would be a proper determination of the rates and pathways of the energy transfers.

Inertial period oscillations were found to be a major element in the temporal variation of the kinetic and potential energies of the system, although they did not appear to seriously affect the frontal evolution at longer than inertial periods. These oscillations grew particularly large in the latter portion of the extended Gulf Stream test. Orlanski and Cox (1977) also found large growth of inertial period oscillations near the end of their model runs. Their results and the present ones suggest that oceanic fronts are sensitive to excitation at this frequency.

The inertial motions were particularly intense where the water velocity was the highest, near the inner/outer boundary. The inner region is a complex zone of turbulent mixing and interleaving and may be able to dissipate the (relatively) high frequency energy in the inertial oscillations and prevent their growth to large amplitude. In

in this investigation the inner region was modeled very simply, with no turbulent energy dissipation occurring within it. Kinetic energy was simply advected across the inner/outer boundary for the non-zero Froude number cases, but the transfer rates were controlled by the inviscid flow in the outer region, not by the inner region flow. The effect of this simple treatment would likely be most important for positive Froude number flows, when water is flowing from the inner region toward the outer region. The inclusion of an inner region with its own dynamics would be an important extension of this model.

Whatever the mechanism for its dissipation, energy at inertial frequencies remains important. Future modeling efforts should be designed with the realization that, unless dispersed, inertial motions can grow to dominate the flow. Corresponding field observations to determine the rate of energy dissipation in the inner region and the direction of the flow across the inner/outer boundary (the sign of the Froude number) are also needed for a better understanding of the dynamics of this region.

These results show the utility of the division of the frontal zone into two regions, turbulent inner and inviscid outer, as suggested by Garvine (1979). The characteristics of the flow in the outer region, such as the conservation of potential vorticity, are the result of inviscid dynamics. However, without a turbulent inner region the entrainment (upward or downward) necessary for a cross stream flow cannot occur. This region is also potentially needed as an energy

sink for inertial period oscillations. Extensions of the present work to include a complete energy analysis and an account of the inner region dynamics would be useful in determining the overall importance of this region. Field studies are also needed to determine the direction and magnitude of the entrainment and the size of the turbulent inner region.

APPENDIX I - COMPUTATIONAL IMPLEMENTATION

A1.1 - Finite Differencing

The numerical algorithm used here is a finite difference scheme based on that proposed by Lax and Wendroff (1960) for the solution of hyperbolic partial differential equations in conservation form. The essential idea of this method is the expansion of the initial equations in a Taylor series, usually with second order accuracy.

Since strong spatial gradients are present in the initial states of all of the cases dealt with here, difficulties were encountered with the numerical scheme. An unmodified Lax-Wendroff approach becomes unstable due to the growth of the second order terms in the regions of strong gradients. Similar difficulties were encountered with several other schemes which were tested (some of which were variants of Lax-Wendroff) because they were not designed to deal with the strong gradients. The method finally chosen is based on an algorithm by Harten and Zwas (1972) intended for computation of compressible flows which include shocks. It is a Lax-Wendroff variant which is second order in smoothly varying regions and is reduced to first order in shock regions. The change from first to second order accuracy is controlled by a variable, α , which Harten and Zwas call an 'automatic switch'. This variable is of order one near a shock and approaches zero in smooth regions. The

second order terms in a Lax-Wendroff scheme are multiplied by the complement of the automatic switch ($1 - \theta$). Thus in smooth regions where θ is small, the scheme will be second order. Near shocks, where θ approaches one, the second order terms will be diminished or eliminated so that the scheme becomes first order. By reducing the relative size of the second order terms, some accuracy is lost near the shock. However, the solutions remain convergent and are not subject to the instabilities introduced at the shock by the second order terms used in other methods. The fact that the present work deals with fronts, which have mild spatial gradients when compared to shocks, does not affect the applicability of this method. However, some problems are encountered with the form of the smoothing or 'artificial viscosity' originally suggested by Harten and Zwas, which shall be discussed below.

The 'automatic switch', θ , has a value near zero in regions of small spatial gradients, and rises to a maximum of unity in the frontal region near the inner/outer boundary. A derivation is given in Harten and Zwas (1972). The form used in this model for the x and y direction switches is:

$$\theta_{i+\frac{1}{2},j}^x = 0.5[|\delta_{i+1,j} - \delta_{i,j}|/\max|\delta_{2+1,j} - \delta_{2,j}|]^2 \quad (\text{A1.1a})$$

$$\theta_{i,j+\frac{1}{2}}^y = 0.5[|\delta_{i,j+1} - \delta_{i,j}|/\max|\delta_{i,2+1} - \delta_{i,2}|]^2 \quad (\text{A1.1b})$$

where $\max | |$ is the maximum difference in the x (or y) direction. The subscripts i and j refer to the x and y axis coordinates of the grid

points. The subscript $\&$ denotes the entire range of the grid along the x or y axis.

The partial differential equation to be solved, written in conservation form is, from (2.4.1)

$$w_t = f_x + g_y + z$$

where w is a column vector and f , g , and z are functions of w . Employing the Jacobians $A = \frac{\partial f}{\partial w}$ and $B = \frac{\partial g}{\partial w}$ we have

$$w_t = Aw_x + Bw_y + z \quad (\text{A1.2})$$

Differentiating (2.4.1) again by t

$$\begin{aligned} w_{tt} &= \left(f_x \right)_t + \left(g_y \right)_t + z_t \\ &= \left(f_t \right)_x + \left(f_t \right)_y + z_t \end{aligned} \quad (\text{A1.3})$$

Inserting the Jacobians, including $C = \frac{\partial z}{\partial w}$

$$w_{tt} = \left(Aw_t \right)_x + \left(Bw_t \right)_y + Cw_t \quad (\text{A1.4})$$

Using (2.4.1) in (A1.4)

$$\begin{aligned} w_{tt} &= [A(f_x + g_y + z)]_x + [B(f_x + g_y + z)]_y \\ &\quad + C(f_x + g_y + z) \end{aligned} \quad (\text{A1.5})$$

The terms on the right hand side of (A1.2) are the first order terms and those on the right hand side of (A1.5) are the second order terms of the Lax-Wendroff scheme. Representing $f_{i+1,j}$ as F^+ , $f_{i-1,j}$ as F^- , $g_{i,j+1}$ as G^+ , etc., and using F^{C+} as $f_{i+1,j+1} + f_{i+1,j} - f_{i-1,j+1} - f_{i-1,j}/4$, etc., the scheme is

$$\begin{aligned}
 w_{i,j}^{n+1} = & w_{i,j}^n + \frac{\Delta t}{2h} (F^+ - F^-) + \frac{\Delta t}{2h} (G^+ - G^-) + \Delta t z \\
 & + \frac{\Delta t}{2h} \left\{ \frac{1}{h} (1 - \theta_{i+\frac{1}{2},j}) A^+ [(F^+ - F) + G^{C+} + \bar{z}^+] \right. \\
 & \left. - \frac{1}{h} (1 - \theta_{i-\frac{1}{2},j}) A^- [(F - F^-) + G^{C-} + \bar{z}^-] \right\} \\
 & + \frac{\Delta t}{2h} \left\{ \frac{1}{h} (1 - \theta_{i,j+\frac{1}{2}}) B^+ [(G^+ - G) + F^{C+} + \bar{z}^+] \right. \\
 & \left. - \frac{1}{h} (1 - \theta_{i,j-\frac{1}{2}}) B^- [(G - G^-) + F^{C-} + \bar{z}^-] \right\} \\
 & + \Delta t^2 \left\{ [1 - \frac{1}{4} (\theta_{i+1,j} + \theta_{i-1,j} + \theta_{i,j+1} + \theta_{i,j-1})] \right. \\
 & \left. C [\frac{1}{2h} (F^+ - F^- + G^+ - G^-) + \bar{z}] \right\} \quad (A1.6)
 \end{aligned}$$

where Δt is the time step and h is the grid spacing which is the same along the x and y axes.

A1.2 - Smoothing

Virtually all finite difference algorithms for fluid dynamic equations employ some form of smoothing or 'artificial viscosity'. The purpose of the smoothing is more a matter of computational stability than an attempt to model actual viscous effects. If fluid viscosity is to be included in a model it is usually incorporated as an additional term in the difference equations. Smoothing effects are usually introduced by comparing the calculated value of a variable at a grid point to an idealized value. The idealized value is commonly taken to be the average of the four nearest neighbors. A smoothing term is computed as a proportion of the deviation of the calculated value from the idealized value. The smoothed value, which is the final result, is the sum of the calculated value and the smoothing term. In most algorithms the proportion of the deviation of the calculated value from the idealized value used to form the smoothing term is the same for all grid points. The Harten and Zwas scheme uses the automatic switch to vary this proportion so that the smoothing is strongest near the shock. The idealized value is still obtained by averaging. Although this method is acceptable for shock computations and for most front models, it could not be used in the present study due to incompatibility of the linear averaging with the curvature of the interfacial depth and velocity fields.

In shock computations the important results are the location and velocity of the shock at a given time. The details of the computed flow within the actual shock region are not considered important, as the shock is expected to form on a small scale in the cross-shock direction.

Ideally, the shock should be sub-grid scale to represent a discontinuity. Thus, in shock regions the error caused by any inaccuracies in the smoothing is not of great importance. Outside of the shock region the flow is expected to be either uniform or slowly varying. In these regions the magnitude of the smoothing term is small. Therefore, models dealing with shock flows which usually employ this averaging technique in the smoothing are not presented with significant problems.

Numerical models of fronts are also able to use this method of smoothing without difficulty due to the assumption of a linear depth profile which is usually made. In this assumption the depth (or height) of the interface is taken to increase linearly with distance away from the surface expression of the front. If an idealized value is computed by averaging, it will lie along the linear profile. With the idealized value being equal (or nearly so) to the initially assumed value, the smoothing terms will act as a force which restores the smoothed value towards the assumed profile (Fig. 21a).

In the present case the interface profile has an exponential variation. If an idealized value for the depth at a given grid point is calculated by averaging, it will not agree with the initially assumed value, but will be towards the 'inside' of the profile curve. A smoothing term based on this type of idealized value will bias the smoothed value away from the initially assumed exponential curve and towards a straight line (Fig. 21b). Unlike the shock computations, the details of the flow in the rapidly changing region are of great importance, and unlike

previous frontal models the averaging technique for obtaining idealized values does not work. Thus, we must derive a method for calculating idealized values which will fit the assumed curve of the depth profile more accurately and will not introduce bias. The exponential curve (4.1.10) used for the initial depth values is a useful shape for use in smoothing.

$$\delta(n_s) = 1 - (1 - \delta_b)e^{-n_s}$$

At each time step this equation is used to predict the depths along each x-directed grid line from the current local front position. These idealized values are subtracted from the calculated depths to form an array of deviations. The smoothing term at each grid point is proportional to the difference between the deviation at that point and the average of the deviations at the two neighboring points.

This method provides a consistent smoothing without introducing a bias. The basic technique may also be used for the along front component of velocity. The velocity is related to the depth by (4.2.5)

$$v = 1 - \delta$$

The same procedure of smoothing according to deviations from a predicted profile is applied along x directed grid lines for the along front velocity to provide a non-biasing smoothing operator. Along y directed grid lines the curves are expected to be sufficiently flat so that linear smoothing may be used for both depth and along frontal velocity.

The component of velocity in the across front direction will have small values and small deviations from a linear profile so that the technique based on averaging neighbors will produce small smoothing terms. This component of velocity will also be very sensitive to small changes in the depth and the other velocity component so that a smoothing method more sophisticated cannot be justified. Thus, the method of averaging nearest neighbors to obtain idealized values is used for this variable.

A1.3 - Extrapolation to Inner Region Points

The scheme detailed in (A1.6) requires values for the three variables at four neighboring points. This presents no difficulty in the center of the grid or at the three boundaries discussed in section 2.4. Points near the free boundary may have nearest neighbors which are in the inner region where no solutions are available from the difference scheme. Therefore, values at grid points in the inner region must be obtained by some other method.

Since the values of the variables are available at the inner/outer boundary; we use a method based on extrapolations from the boundary. The position of the boundary at each x directed grid line is determined by a linear fit to the two nearest neighbors to the grid line. Values for the variable for the two components of velocity are obtained in a similar manner. The depth extrapolated to points in the inner region is determined by (4.1.10). Since the difference scheme (A1.6) actually uses mass flux values instead of velocities, the velocities at inner

region grid points are determined by matching mass flux values to the boundary. That is, the grid point velocities are chosen so that the mass flux at the grid point is equal to that at the interpolated boundary point.

APPENDIX II - OTHER COMPUTATIONAL TECHNIQUES

AII.1 - Depth Derivatives at the Free Boundary

At each drift point on the free boundary the depth derivatives are required to compute the acceleration terms in (3.3.1). These derivatives are calculated from the surrounding grid point depths. Since the drift points are usually not on the grid lines, the technique used for the grid point derivatives of differencing nearest neighbors cannot be applied directly. The method used must be based either on interpolation or extrapolation. Two approaches, one of each of these types, have been tested for use in this model.

The first method tested was an extrapolation technique based on that used by Kasahara et al. (1965). In the case examined by Kasahara et al. the cross stream flow was assumed to be zero and there was no region of turbulent entrainment. Therefore, the frontal layer was not divided into inner and outer regions as is done here, and the thickness of the frontal layer was taken to be zero at the free boundary. Since the free boundary was then entirely outside of the frontal layer, extrapolation was required.

The extrapolation procedure used for this model involves constructing a line which is locally normal to the front at the boundary point for which the derivatives are being computed. The method of

constructing the normal line is discussed in AII.2. The points at which the normal line crosses grid lines in the frontal region are noted, and from these a base point is selected. The base point is the point closest to the front which has at least three of its four nearest neighbors on the same grid line inside the frontal region (type 1 or 2 points - see AII.2). Values for the depth and the x and y derivatives of the depth are obtained at the base point by interpolation from the three neighbors. From these values and the known depth at the boundary, least squares quadratic fits are made. The x and y components of the depth derivatives at the boundary point are computed from the fitted curves.

In the present model this procedure was found to yield poor quality results. The calculated derivatives were not smoothly varying along the front and were occasionally not within acceptable error bounds. The reasons for the success of this algorithm in the Kasahara et al. study and its failure here are largely attributable to the difference between the exponential interface used here and the linear interface assumed for the earlier study. Large variations in interfacial slope with distance from the front exist for an exponential profile, not all of which can be accommodated by a polynomial fit. Since the various derivatives are extrapolated from points at differing distances from the front, divergent slope estimates were obtained. The extrapolation procedure is also computationally expensive. To surmount these problems, a second scheme was devised which uses the depths which are available in the inner region in an interpolation.

A boundary point may be viewed as being inside a square with a grid point at each corner. For an x derivative, two pairs of grid points are formed by taking points on the same x directed grid line to be a pair. An x derivative is formed for each pair and these are linearly interpolated to the boundary point. The same procedure is used for y derivatives with the pairs being formed along y directed grid lines. This procedure gives stable and consistent values and is used for all of the model runs.

AII.2 - Grid Point Status Determination

As discussed above, grid points on one side of the inner/outer boundary (in the inner region, Appendix I) are treated differently than points on the other side of the boundary (in the outer region, Chapter 2). Since the inner/outer boundary can move, a grid point initially on one side of the boundary can be on the other side at some later time by having the boundary move across it. The model must therefore keep track of the position of the boundary relative to each grid point (the grid point status) at each time step.

The technique used here to determine the status of a grid point follows the method of Neumann and Sproull (1979). This approach is based on a mapping of a point in a two dimensional Cartesian space to a vector in a three dimensional space. The point (x, y) may be represented by (wx, wy, w) with $w \neq 0$. Taking two points

$$p = (p_1, p_2, p_3)$$

$$v = (v_1, v_2, v_3)$$

the line between them, from p to v , may be expressed as the vector

$$\gamma = \begin{bmatrix} a \\ b \\ c \end{bmatrix} = \begin{bmatrix} p_2v_3 - p_3v_2 \\ p_3v_1 - p_1v_3 \\ p_1v_2 - p_2v_1 \end{bmatrix} = pxv \quad (\text{AII.2.1})$$

The position of a third point, $r = (r_1, r_2, r_3)$, with respect to γ may be determined by taking the dot product $r \cdot \gamma$. If $r \cdot \gamma = 0$, then r is on the line. If r is to the right of the line looking from p to v , then $r \cdot \gamma$ will be negative; if r is to the left then $r \cdot \gamma$ will be positive. The perpendicular distance from r to γ is given by

$$d = (r \cdot \gamma) / [r_3(a^2 + b^2)^{1/2}] \quad (\text{AII.2.2})$$

In the model, the two boundary points closest to the grid point of interest are chosen and the boundary is represented by the straight line between them. Since the boundary point spacing is very small compared to the scale of the disturbance, the use of a linear fit does not introduce a significant error.

This procedure for determining the distance from the front to a grid point is also used in the determination of the depth field in the inner region (see Appendix I). The errors introduced for this computation by the straight line approximation have been tested and shown to be small.

To keep track of the numerous grid points, a set of numeric designations has been adopted. The five types of grid points are:

Type 1 - a point in the outer region whose four nearest neighbors are also in the outer region.

Type 2 - a point in the outer region which is at least 1/4 of a grid unit away from the boundary, but which does not have all of its four nearest neighbors in the outer region.

Type 3 - same as type 2 except that it is within 1/4 of a grid unit of the boundary.

Type 4 - a point outside the outer region, at least one of whose neighbors is in the outer region.

Type 5 - a point outside the outer region, all of whose neighbors are outside the outer region.

The time steps used in the model are small enough so that the position of the front changes by much less than 1/4 of a grid unit in a cycle. Therefore, the status of any point will not change more than one classification in a cycle.

The technique of mapping a point from two to three-space is also used in the determination of the derivatives of the depth field at the frontal boundary for the extrapolation method discussed above. Two of the manipulations required for that operation are locating the point of intersection of two lines, and constructing a line normal to a given line. The point of intersection of two lines γ and ω is found by taking the cross product of the transpose of the two vectors

$$s = \omega^T \times \gamma^T \quad (\text{AII.2.3})$$

Note that, when remapped into two-space,

$$-s = \gamma^T \times \omega^T \quad (\text{AII.2.4})$$

is the same point as s .

For γ and ω to be perpendicular, we must have

$$(\gamma^T J) \cdot \omega = 0 \quad (\text{AII.2.5})$$

where

$$J = \begin{vmatrix} 1 & 0 & 0 \\ 0 & 1 & 0 \\ 0 & 0 & 0 \end{vmatrix}$$

The line Ω which is normal to γ and passes through the point $v = (v_1, v_2, v_3)$ is

$$\hat{n} = \begin{vmatrix} bv_3 \\ -av_3 \\ (av_2 - bv_1) \end{vmatrix} \quad (\text{AII.2.6})$$

AII.3 - Redistribution of Points Along the Boundary

The quasi-Lagrangian drift points which mark the position of the free boundary are initially distributed approximately evenly along the length of the boundary. Later, when the front has evolved, the drift

points may become clustered in some regions and widely spaced in others. If the spacing gets to be too uneven, it becomes advisable to redistribute the points along the boundary. This type of problem is common to Lagrangian models. Fortunately, in this case the rezoning can be performed as a one dimensional problem, whereas most Lagrangian flow models must be rezoned in two dimensions.

The rezoning is applied along the length of the boundary and results in a new set of y axis coordinates for the drift points. These new positions are then used with a series of fitted curves to determine the corresponding x axis coordinates for the drift points. Since the drift points will begin to shift as soon as the model execution is resumed, the rezoning of the y axis coordinates does not need to be precise. However, once the new y coordinates are chosen, the x coordinates must be determined accurately.

A segmented front is established as a series of straight line segments between the points on the evolved boundary. The average interval spacing is computed by summing the lengths of all of the line segments and dividing by the number of intervals. A new set of points is then established along the segmented front, distributed evenly at the average interval spacing. The y axis coordinates of these points are used as the rezoned y coordinates.

A cubic spline fit is then made to the unmodified evolved boundary points. Rezoned x coordinates are interpolated at the rezoned y positions using this fit. Thus, the rezoned points are distributed evenly along

the length of the boundary (by the choice of y coordinates) and determine a boundary with the same shape as the original (by the determination of the x coordinates). The new velocity components are determined by the same method of interpolation from a cubic spline fit as the x coordinates.

REFERENCES

- Assaf, G., 1977. The Gulf Stream: Inertia and friction. Tellus 29: 137-143.
- Backus, R. H., J. E. Craddock, R. L. Haedrich, and D. L. Shores, 1969. Mesopelagic fishes and thermal fronts in the western Sargasso Sea. Marine Biol. 3: 87-106.
- Bernstein, R., L. Breaker, and R. Writner, 1977. California Current eddy formation: Ship, air and satellite results. Science 195: 4276-4278.
- Collins, C. A., C. N. K. Mooers, M. R. Stevenson, R. C. Smith, and J. G. Patullo, 1968. Direct current measurements in the frontal zone of a coastal upwelling region. J. Oceanogr. Soc. Japan 24: 295-306.
- Cromwell, T. and J. L. Reid, 1956. A study of oceanic fronts. Tellus 8: 94-101.
- Duxbury, A. C., 1963. An investigation of stable waves along a velocity shear boundary in a two layer sea with a geostrophic flow regime. J. M. R. 21: 246-283.
- Formato, R. A., 1979. Wavelike baroclinic disturbances on shallow upper ocean density fronts. C. M. S. Rept. CMS-C-1-79.
- Fuglister, F. C. and L. V. Worthington, 1951. Some results of a multiple ship survey of the Gulf Stream. Tellus 3: 1-14.
- Gall, R., 1976. A comparison of linear baroclinic instability theory with the eddy statistics of a general circulation model. J. A. S. 33: 349-373.
- Garvine, R. W., 1974. Dynamics of small-scale oceanic fronts. J. P. O. 4: 557-569.
- Garvine, R. W., 1979a. An integral hydrodynamic model of upper ocean frontal dynamics: Part I. Development and analysis. J. P. O. 9: 1-18.

- Garvine, R. W., 1979b. An integral hydrodynamic model of upper ocean frontal dynamics: Part II. Physical characteristics and comparison with observations. J. P. O. 9: 19-36.
- Garvine, R. W. and J. D. Monk, 1974. Frontal structure of a river plume. J. G. R. 79: 2251-2259.
- Grammeltvedt, A., 1970. Numerical simulation of the motion of atmospheric fronts using a two layer model. Tellus 22: 625-637.
- Halliwell, G. and C. N. K. Mooers, 1979. The space-time structure and variability of the shelf water/slope water and Gulf Stream thermal fronts and warm core eddies off the northeast U. S. submitted to J. G. R.
- Hansen, D. V., 1970. Gulf Stream meanders between Cape Hatteras and the Grand Banks. Deep Sea Res. 17: 495-511.
- Haurwitz, B. and H. A. Panofsky, 1950. Stability and meandering of the Gulf Stream. Trans. Am. Geophys. Union 31: 723-731.
- Hoskins, B. J. and F. P. Bretherton, 1972. Atmospheric frontogenesis models: Mathematical formulation and solution. J. Atmos. Sci. 29: 11-37.
- Houghton, D., 1969. Effect of rotation on the formation of hydraulic jumps. J. G. R. 74: 1351-1360.
- Kasahara, A., E. Issacson, and J. J. Stoker, 1965. Numerical studies of frontal motion in the atmosphere: I. Tellus 17: 261-276.
- Kasahara, A. and D. Rao, 1972. Instability of frontal motions in the atmosphere. J. Atmos. Sci. 29: 1090-1108.
- Katz, E. J., 1969. Further study of a front in the Sargasso Sea. Tellus 21: 259-269.
- Kao, T. W., 1980. The dynamics of oceanic fronts. Part I: The Gulf Stream. J. P. O. 10: 483-492.
- Lipps, F. B., 1963. Stability of jets in a divergent barotropic fluid. J. Atmos. Sci. 20: 120-129.
- Neumann, W. F. and R. F. Sproull, 1979. Principles of interactive computer graphics. 2nd ed. McGraw Hill, N. Y.
- Newton, C. W., 1978. Fronts and wave disturbances in Gulf Stream and atmospheric Jet Stream. J. G. R. 83: 4697-4706.

- Orlanski, J. 1968. Instability of frontal waves. J. Atmos. Sci. 25: 178-200.
- Orlanski, I., 1969. The influence of bottom topography on the stability of jets in a baroclinic fluid. J. Atmos. Sci. 26: 1216-1232.
- Orlanski, I., 1976. A simple boundary condition for unbounded hyperbolic flows. J. Comp. Phys. 21: 251-269.
- Orlanski, I. and M. D. Cox, 1973. Baroclinic instability in ocean currents. G. F. D. 4: 297-332.
- Orlanski, I. and B. B. Ross, 1977. The circulation associated with a cold front. J. Atmos. Sci. 34: 1619-1633.
- Pedlosky, J., 1975. On secondary baroclinic instability and the meridional scale of motion in the ocean. J. P. O. 5: 603-607.
- Pedlosky, J., 1979. Finite amplitude baroclinic waves in a continuous model of the atmosphere. J. Atmos. Sci. 36: 1908-1924.
- Pedlosky, J., 1979. Geophysical fluid dynamics. Springer-Verlag. New York. 623 p.
- Robinson, A. R., 1971. The Gulf Stream. Phil. Trans. Roy. Soc. London A 270: 351-370.
- Robinson, A. R., J. R. Luyten, and F. C. Fuglister, 1974. Transient Gulf Stream meandering: Part I. An observational experiment. J. P. O. 4: 237-255.
- Saltzman, B. and C-M. Tang, 1975. Formation of meanders, fronts, and cutoff thermal pools in a baroclinic ocean current. J. P. O. 5: 86-92.
- Simmons, A. J. and B. J. Hoskins, 1978. The life cycles of some non-linear baroclinic waves. J. Atmos. Sci. 35: 414-432.
- Simmons, A. J. and B. J. Hoskins, 1979. The downstream and upstream development of unstable baroclinic waves. J. Atmos. Sci. 36: 1239-1254.
- Stoker, J. J., 1953. Dynamical theory for treating the motion of cold and warm fronts in the atmosphere. N. Y. U. Rept. IMM-NYU-195.
- Stoker, J. J., 1957. Water waves. Interscience. New York. 567 p.
- Stommel, H., 1976. The Gulf Stream. U. of Calif. Press. Berkeley. 248 p.

- Tareev, B. A., 1965. Unstable Rossby waves and the instability of oceanic currents. Fiz. Atm. Ocean. Akad. Nauk. 1: 250-256.
- Thacker, W. C., 1976. Spatial growth of Gulf Stream meanders. Geophys. Fluid Dyn. 7: 271-295.
- Turkel, E., 1974. Frontal motion in the atmosphere. Tellus 26: 630-637.
- Voorhis, A. D. and J. B. Hersey, 1964. Oceanic thermal fronts in the Sargasso Sea. J. G. R. 69: 3809-3817.
- Voorhis, A. D., 1969. The horizontal extent and persistence of thermal fronts in the Sargasso Sea. Deep Sea Res. Suppl. 16: 331-337.
- Webster, F., 1961. The effect of meanders on the kinetic energy balance of the Gulf Steam. Tellus 13: 392-401.
- Whitham, G. B., 1953. Dynamics of meteorological fronts. N. Y. U. Rept. IMM-NYU-195.

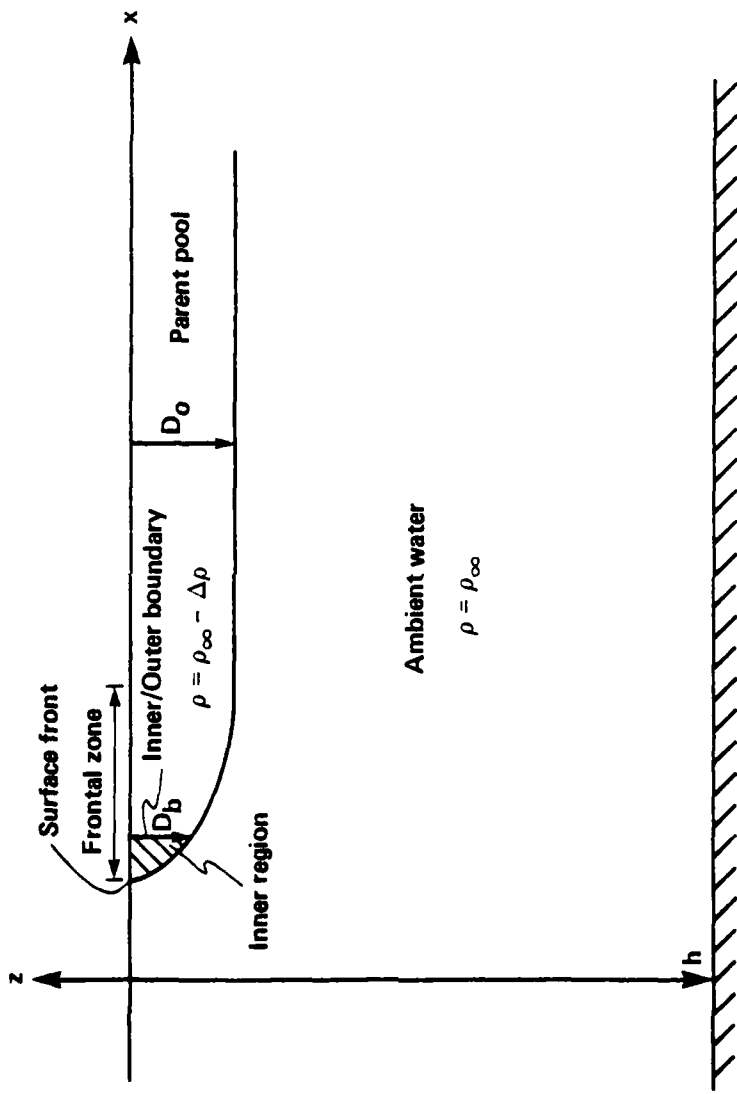


Figure 1. A section in a vertical plane across the front showing the division of the area into the ambient region and the inner and outer frontal regions. The unperturbed surface front lies parallel to the y axis (into the page).

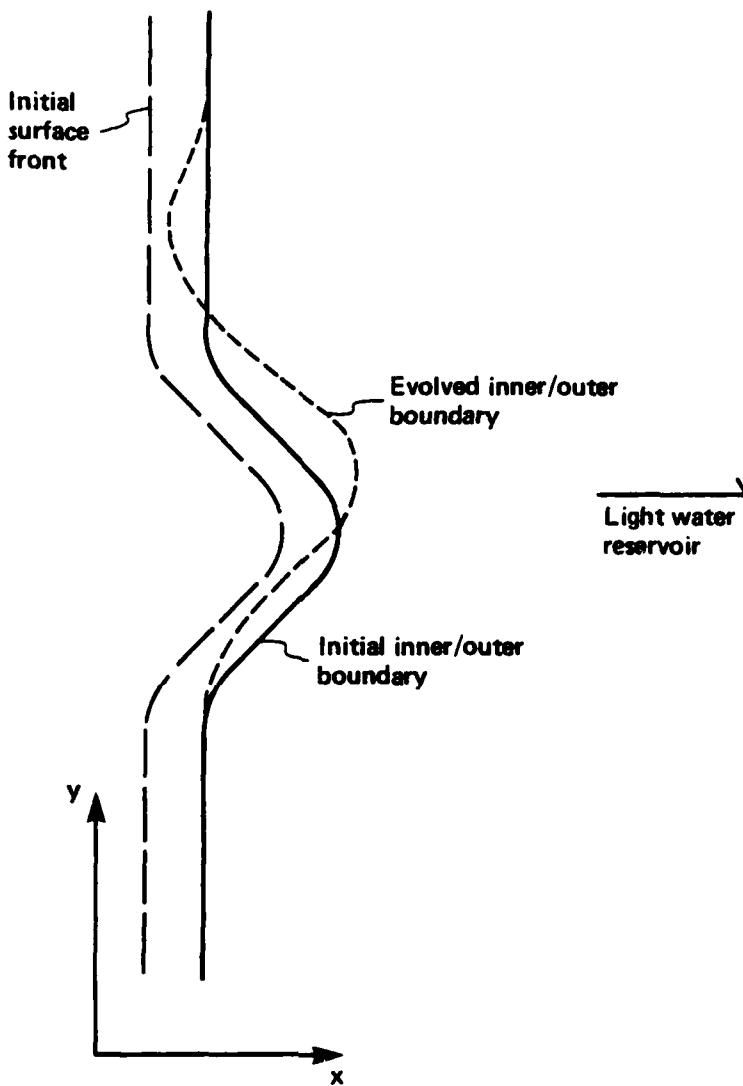


Figure 2. Plan view of the initial perturbed position of the inner/outer boundary and the surface front, and the position of the inner/outer boundary at a later time after frontal evolution.

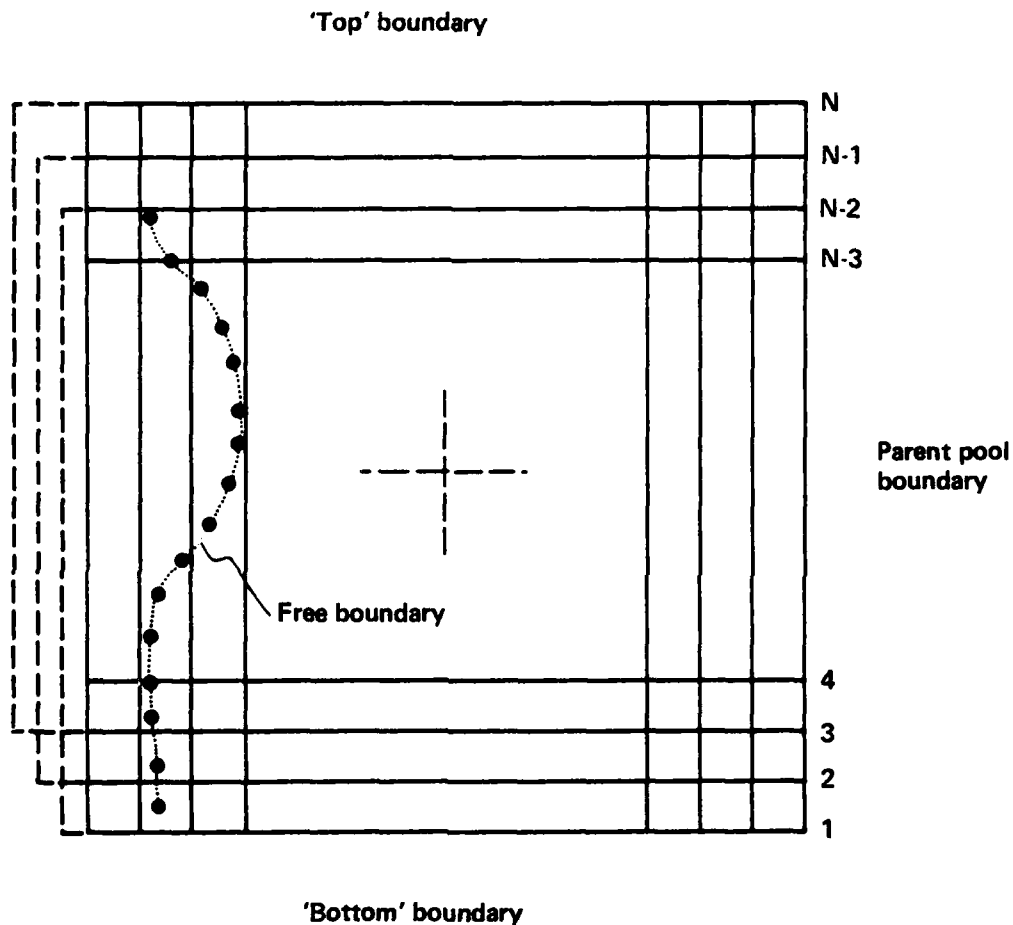


Figure 3. Model grid showing the positions of the boundaries. The dotted line through the solid circles (quasi-Lagrangian drift points) shows the position of the free boundary. The dashed lines show equivalent pairs of grid lines which make the top and bottom boundaries periodic.

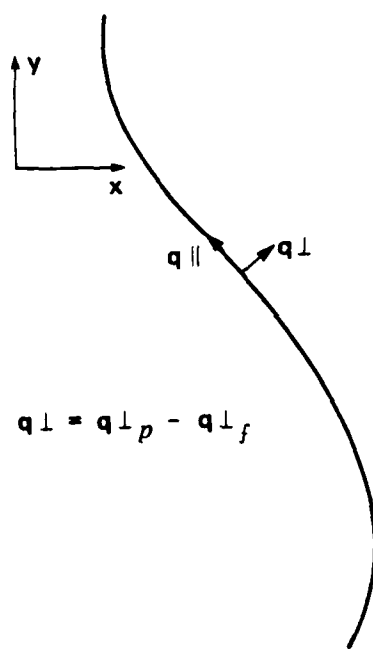


Figure 4. A section of the free boundary showing the velocity components. The component of velocity perpendicular to the front, \mathbf{q}_{\perp} , is controlled by the particle velocity, $\mathbf{q}_{\perp p}$, and the velocity due to the mass flux, $\mathbf{q}_{\perp f}$.

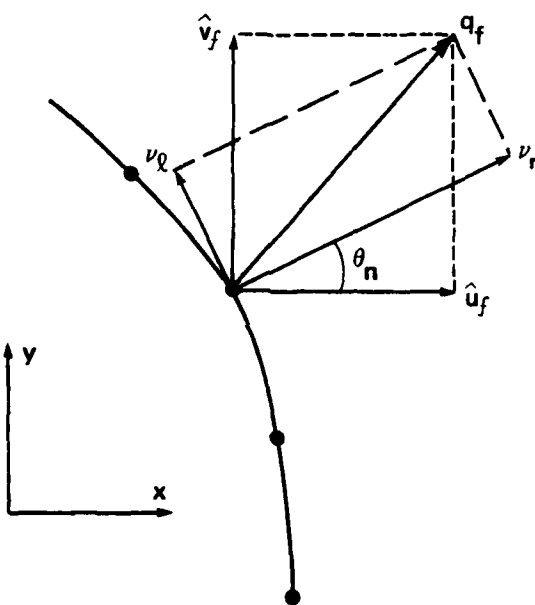


Figure 5. A section of the free boundary showing the mass flux velocity components. The grid oriented velocities, \hat{u}_f and \hat{v}_f , are components of the flux velocity, q_f , which is equal to the sum of v_r and v_l , the boundary perpendicular and parallel velocities.

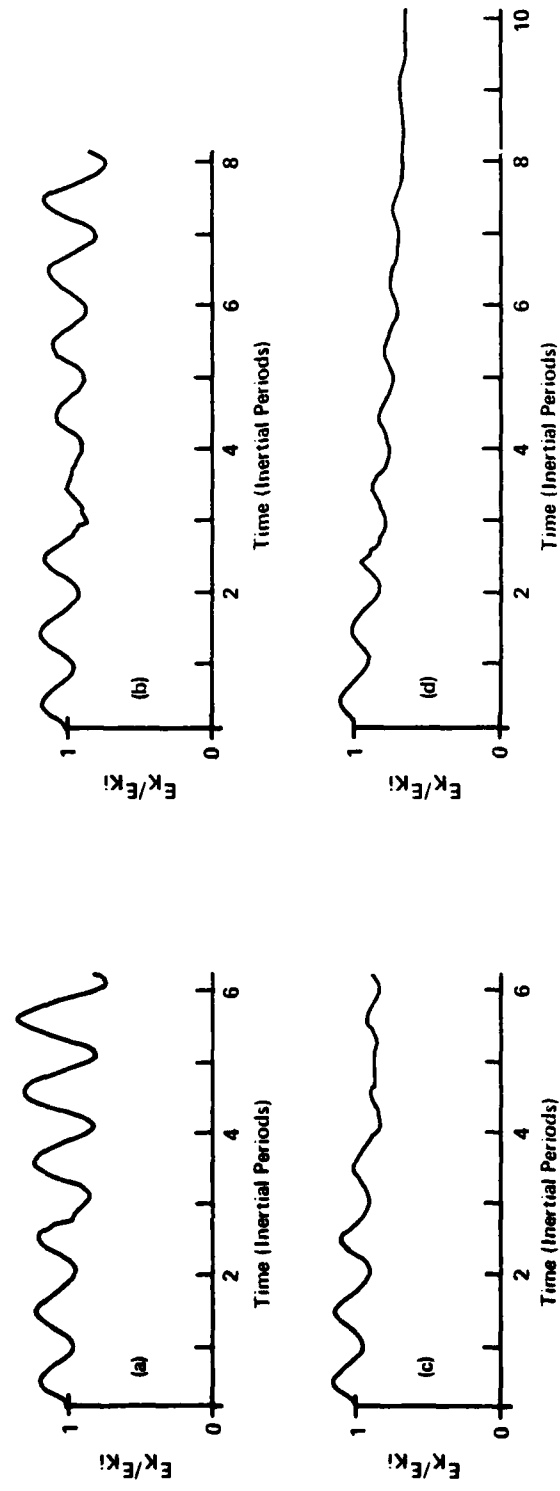


Figure 6. Normalized energy vs. time (in inertial periods) for various values of the friction coefficient: a) 0.001, b) 0.0015, c) 0.002, d) 0.004.

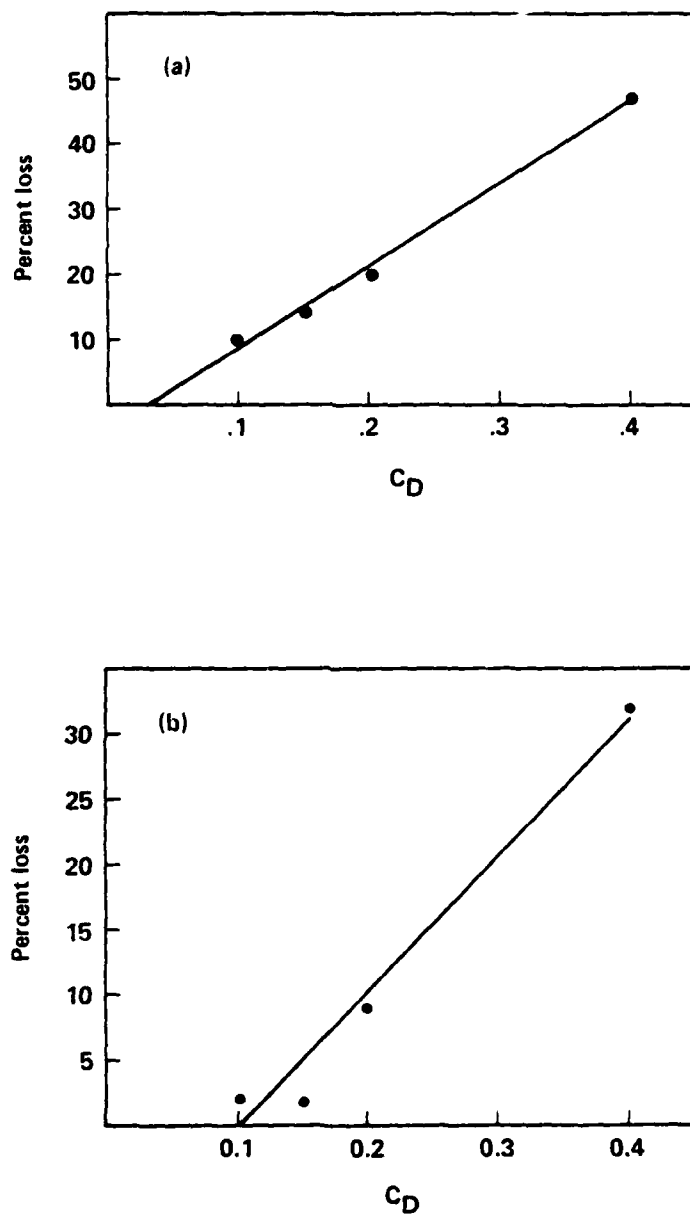


Figure 7. Losses of a) kinetic energy and b) potential energy due to interfacial friction.

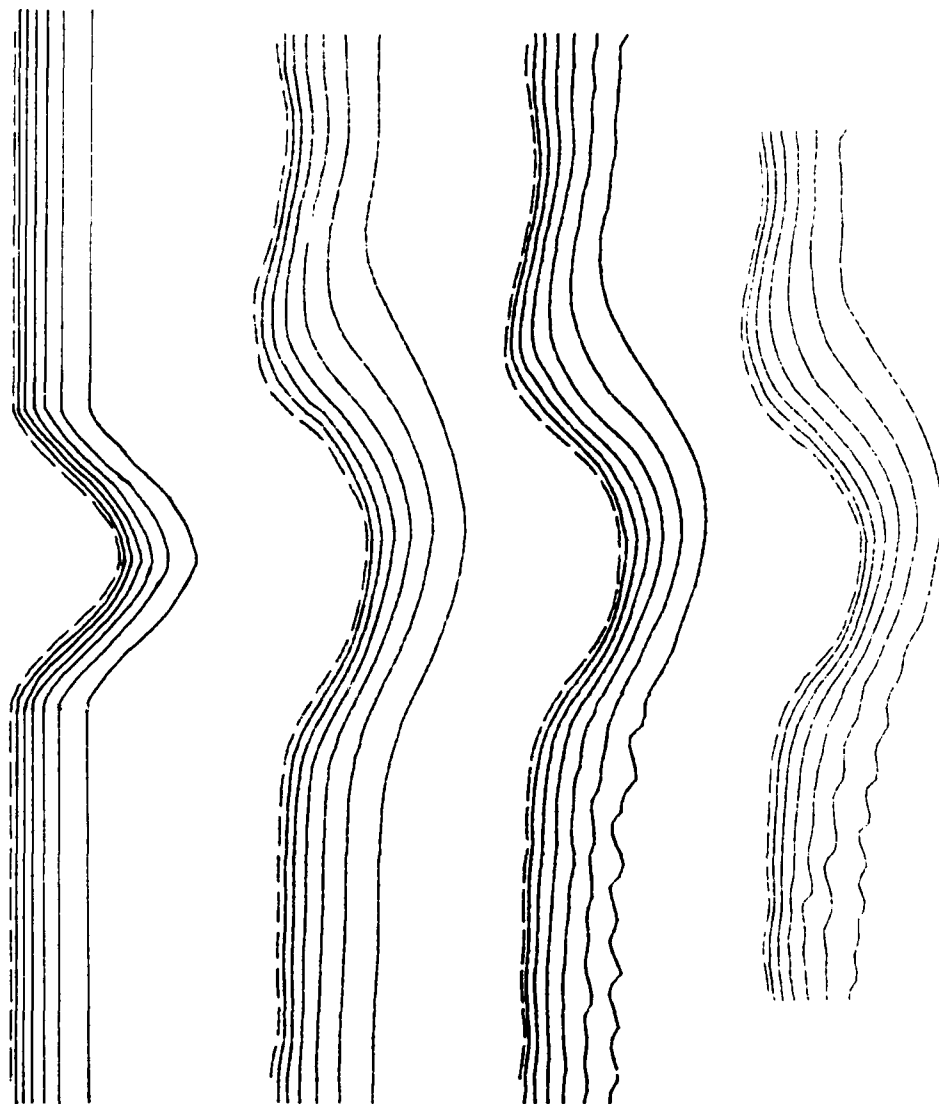


Figure 8. Depth contours for the standard case and two comparison cases. Dashed lines show free boundary position, $\delta = \delta_B = 0.33$. Solid lines are contours at $\delta = 0.4, 0.5, 0.6, 0.7, 0.8$, and 0.9 . The four plots are for: a) initial state, b) grid sensitivity case, c) standard case, d) time step sensitivity case, all cases after ten inertial periods.

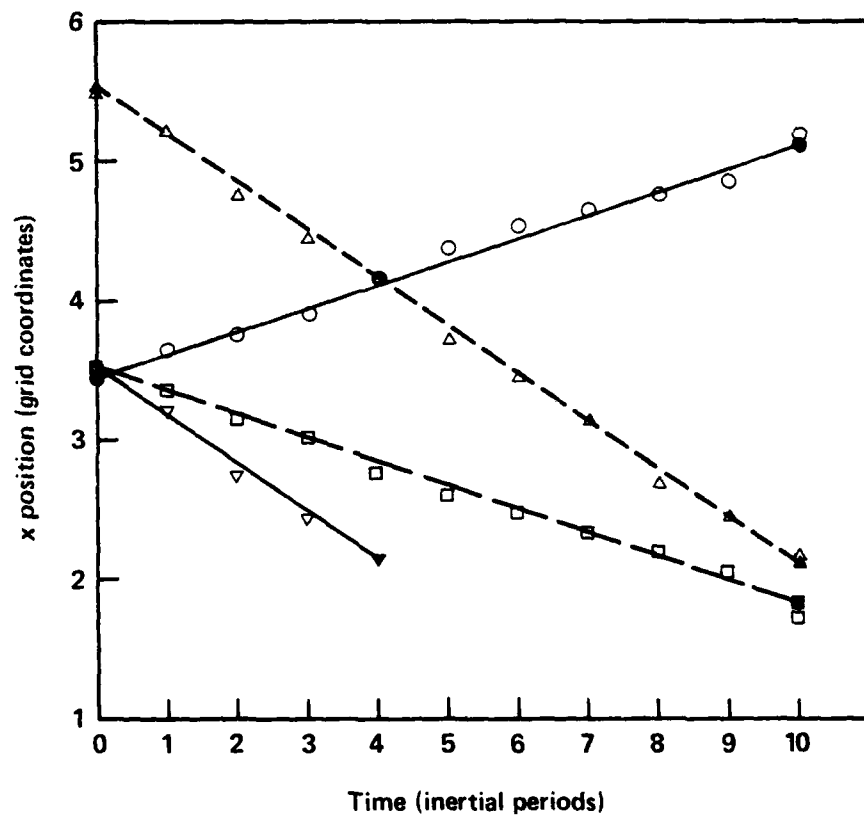


Figure 9. Frontal position vs. time for unperturbed front with varying cross stream Froude numbers. $F_r = -0.02$, $F_c = 0.0$, $F_c = 0.01$ initially at $x = 3.5$, $F_c = 0.01$ initially at $x = 5.5$. Solid symbols and connecting lines show the corresponding linear fits to the frontal positions.

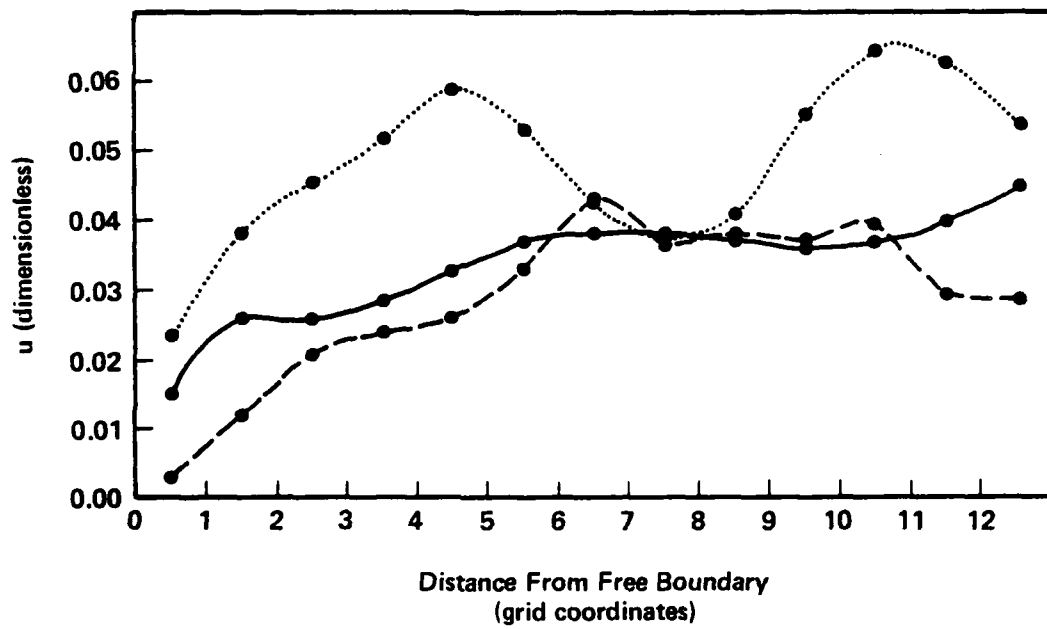


Figure 10. Cross stream velocity across the frontal region for the unperturbed front after ten inertial periods. The solid line is for $F_r = 0.0$, the dotted line is for $F_r = 0.01$ and the dashed line is for $F_r = -0.02$.

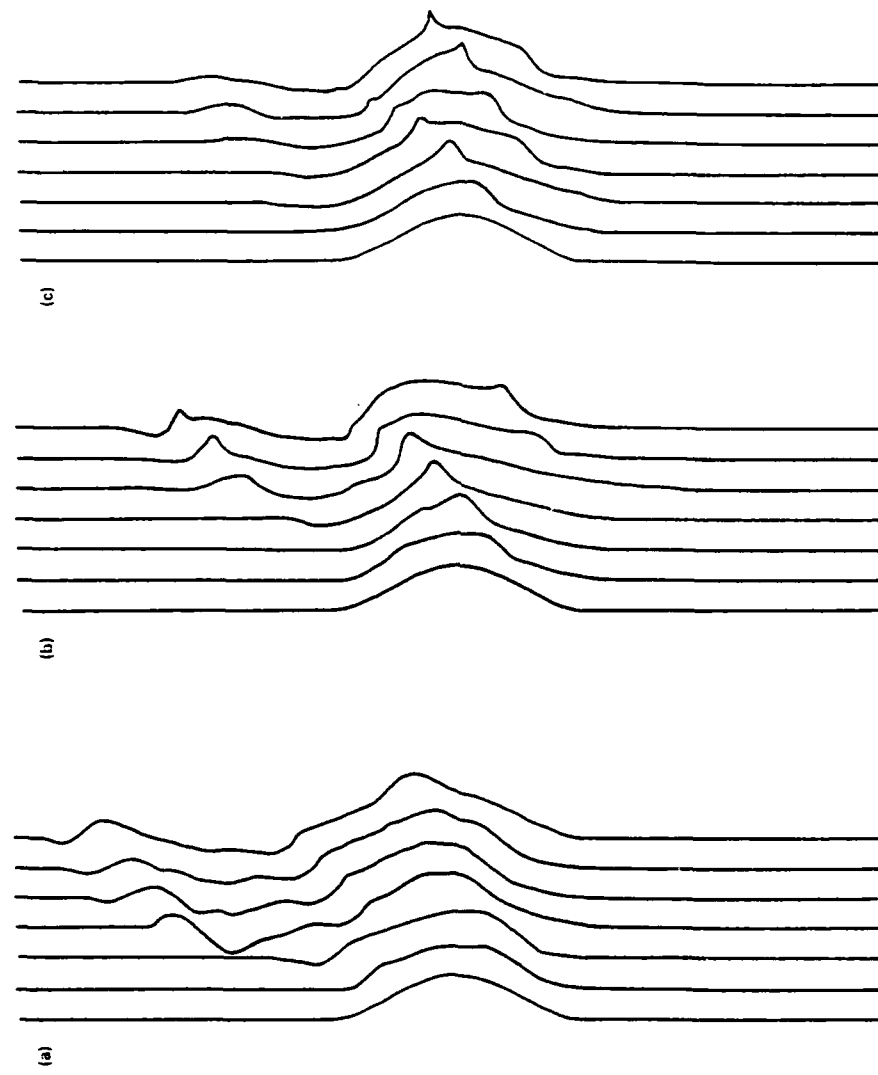


Figure 11. Time sequence of frontal position. The leftmost curve of each shows the initial disturbance. Time advances to the right with each curve being successively one inertial period later. The x scale for each curve has been expanded by a factor of five to enhance the visibility of the small amplitude perturbations. The three sets are for: a) $F_r = -0.02$, b) $F_r = 0.00$ c) $F_r = 0.01$.

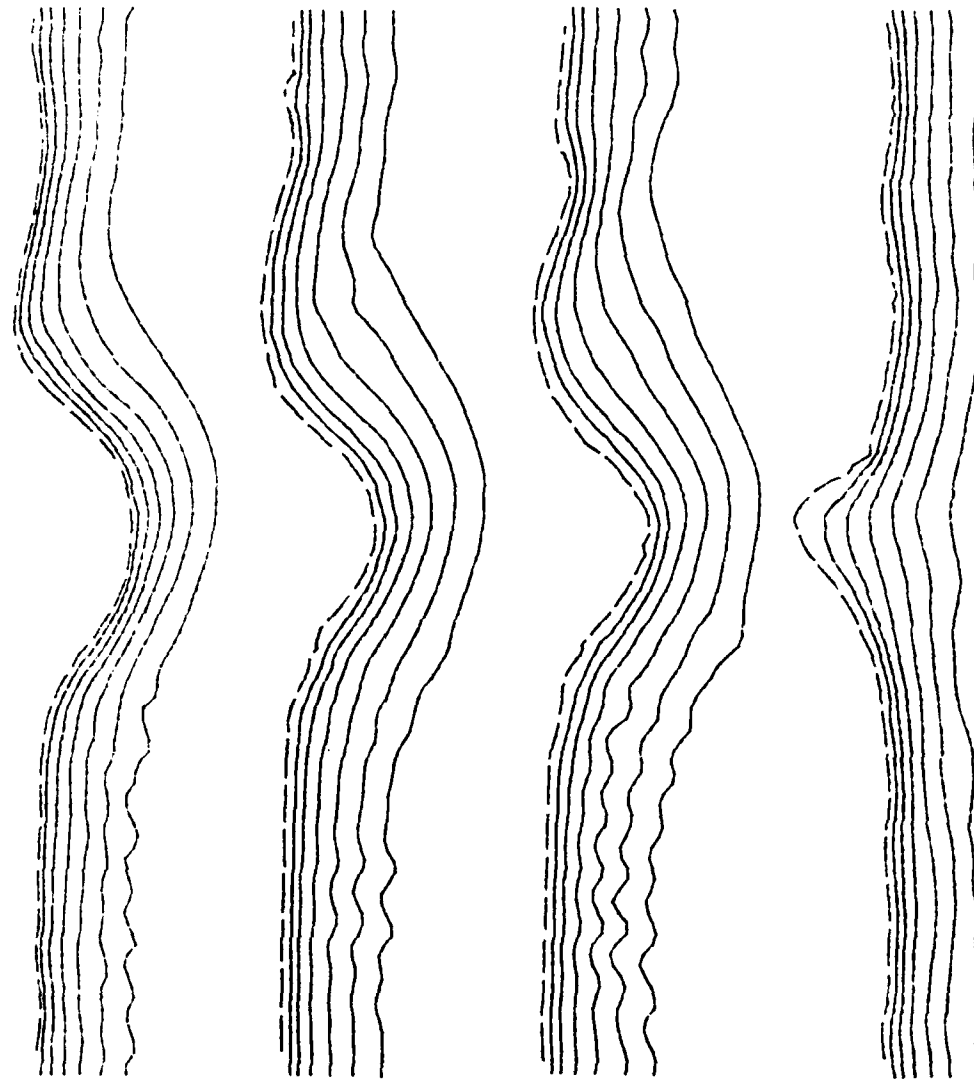


Figure 12. Depth contours, large amplitude perturbation. The four plots are for a) $F_r = -0.02$, b) $F_r = 0.00$, c) $F_r = 0.01$, and d) $F_r = -0.02$, inverted bulge.

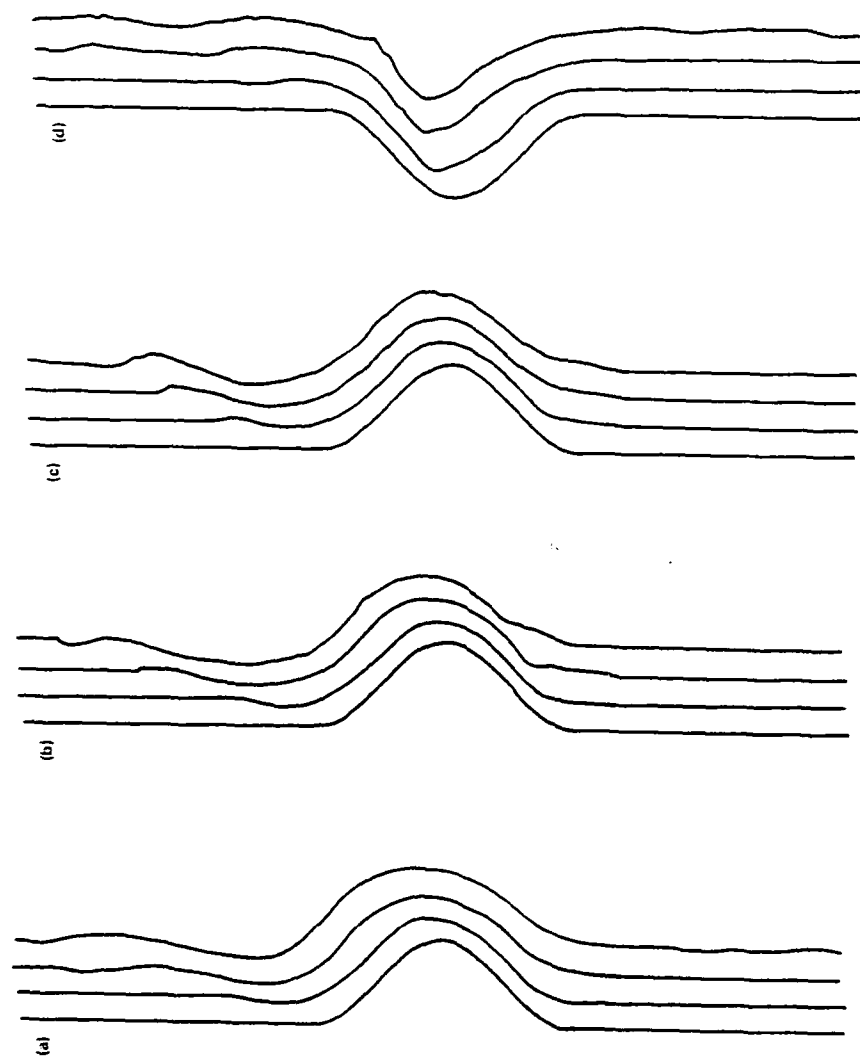


Figure 13. Time sequence of frontal position, large amplitude disturbance. Time advances to the right. Curves are for 0, 2, 6, and 10 inertial periods.

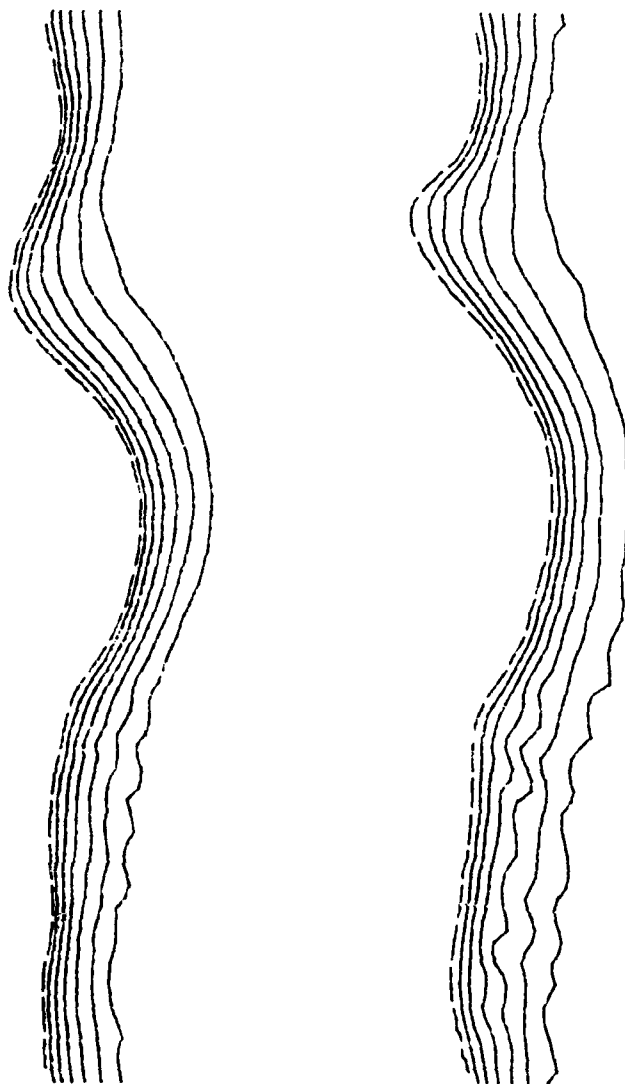


Figure 14. Depth contours large amplitude disturbance extended run. Curves are for a) 18 and b) 34 inertial periods.

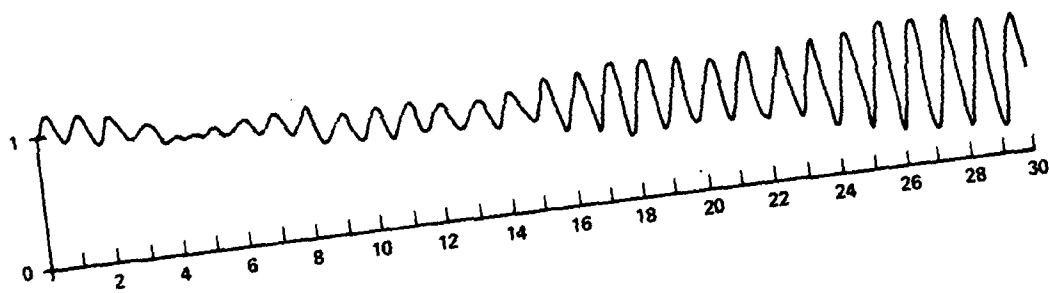
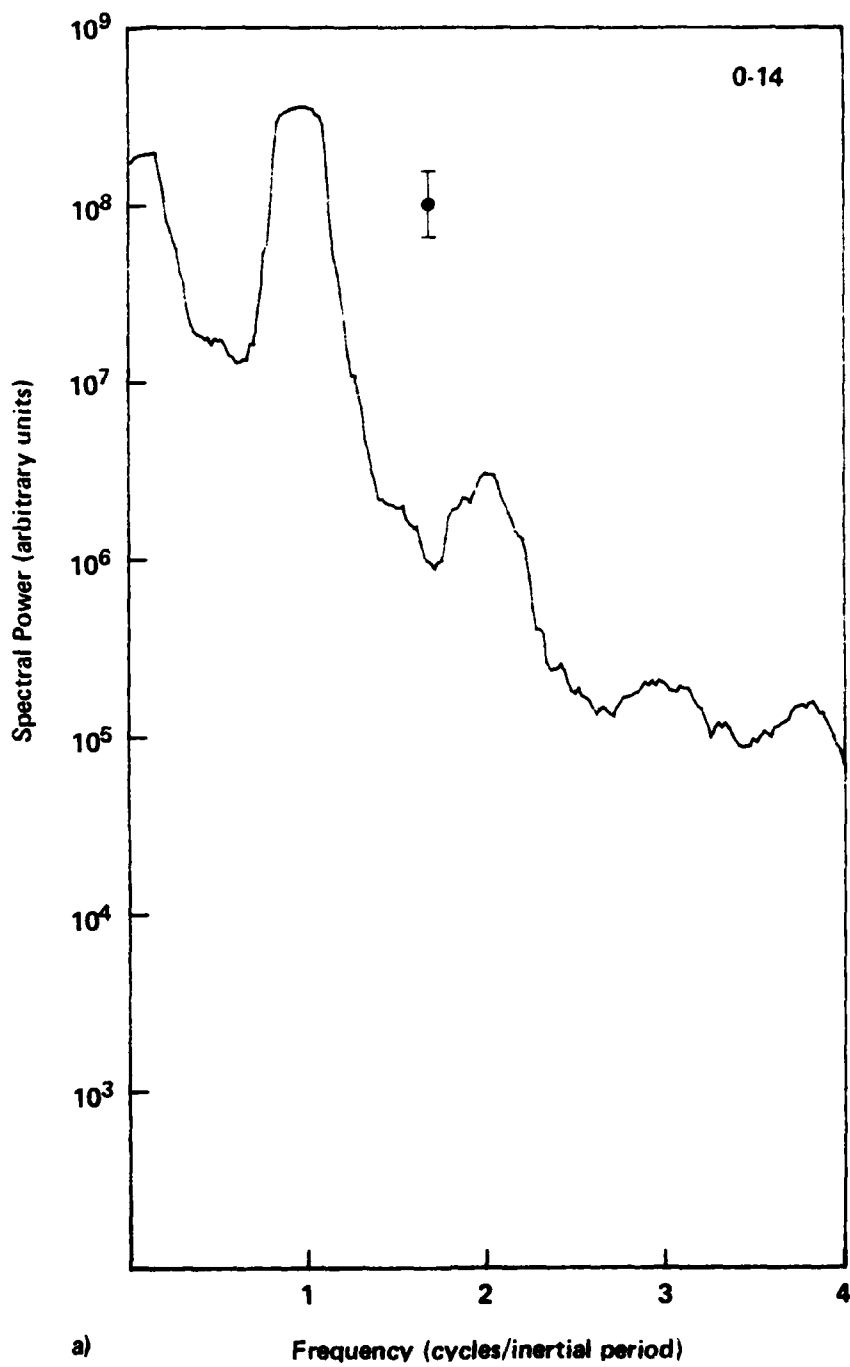


Figure 15. Normalized kinetic energy vs. time (in inertial periods) for the extended large amplitude disturbance test.



a)

Frequency (cycles/inertial period)

Figure 16a. Spectra obtained from the normalized kinetic energy (Fig. 15). 0-14 inertial periods. Spectral power units are arbitrary due to the original data being normalized.

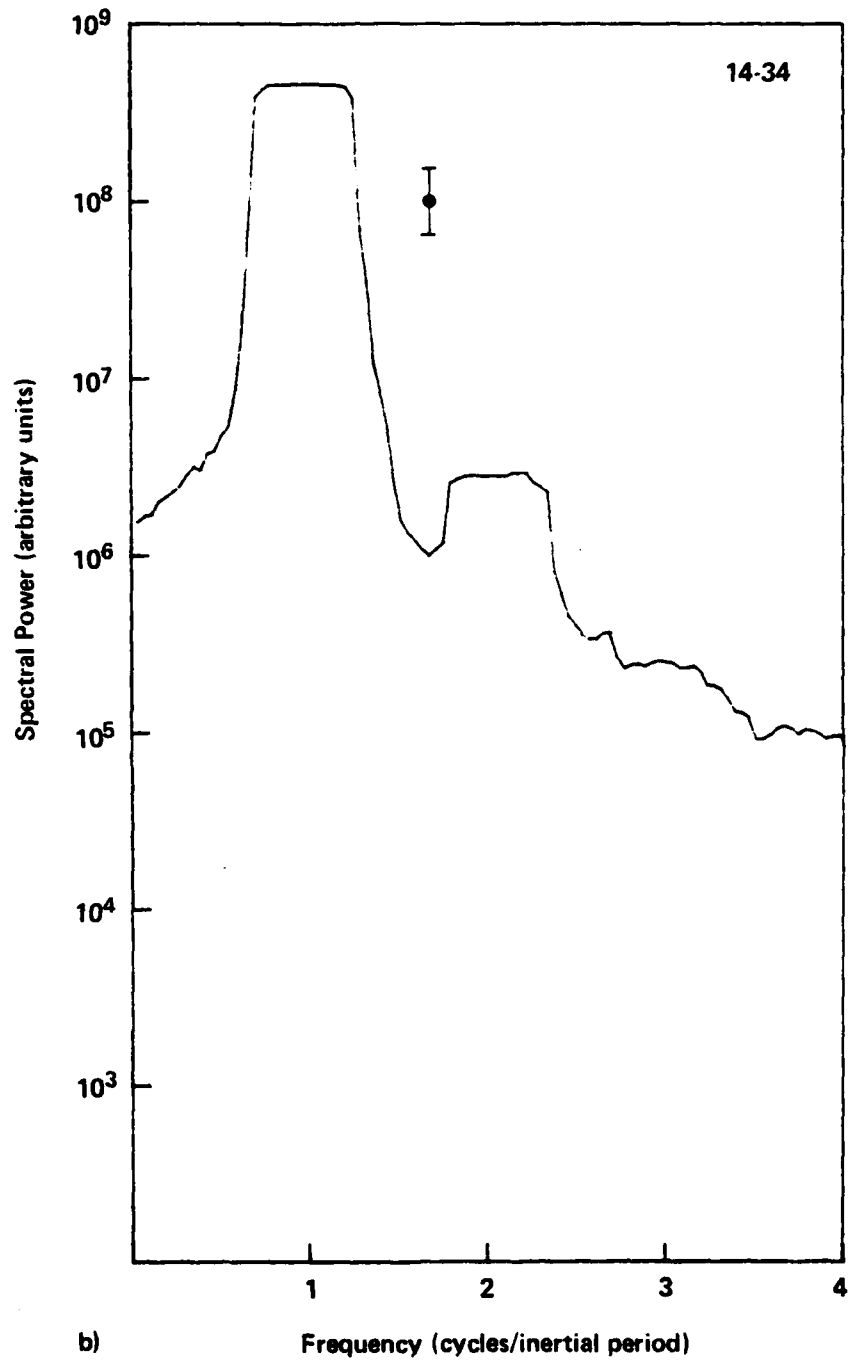


Figure 16b. Spectra obtained from the normalized kinetic energy (Fig. 15). 14-34 inertial periods. Spectral power units are arbitrary due to the original data being normalized.

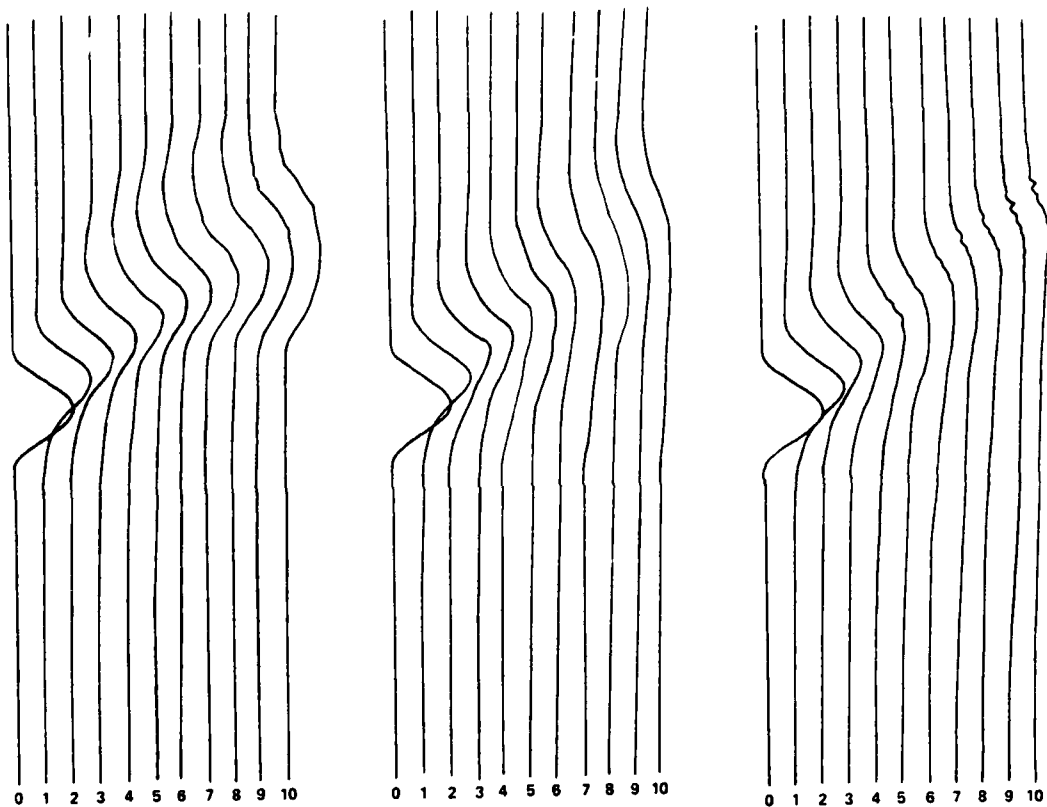


Figure 17. Time series of frontal position for the Sargasso Sea short wavelength tests, a) $F_r = -0.02$, b) $F_r = 0.00$, c) $F_r = 0.01$. Time advances to the right at one inertial period intervals. The x scale for each curve has been expanded by a factor of five.

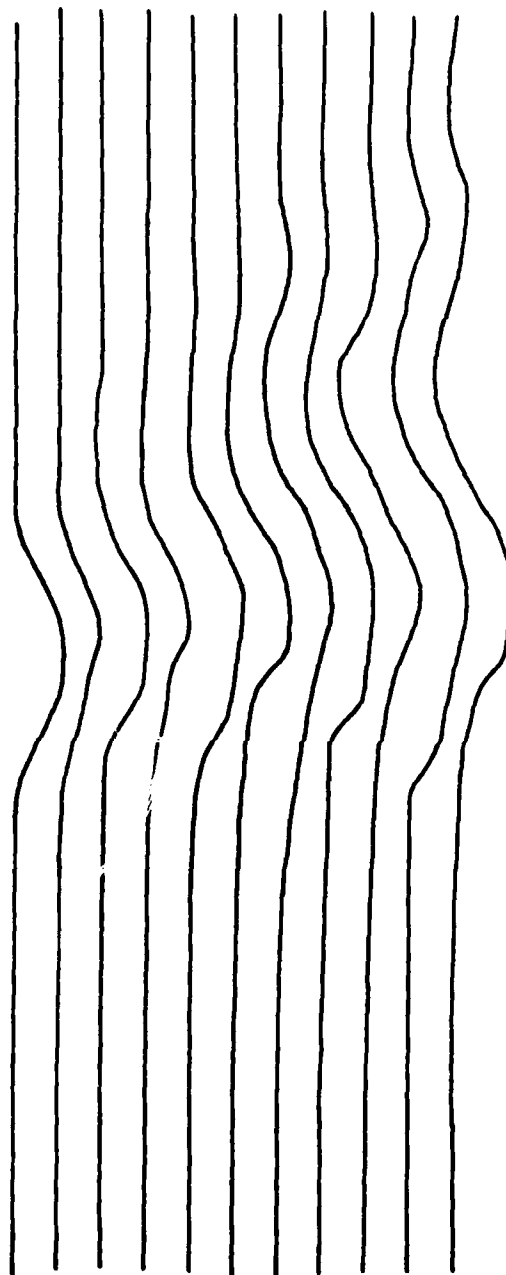


Figure 18. Time sequence of frontal position for the Sargasso Sea long wavelength 3 km amplitude test. Time advances to the right at one inertial period intervals. The x scale for each curve has been expanded by a factor of five.

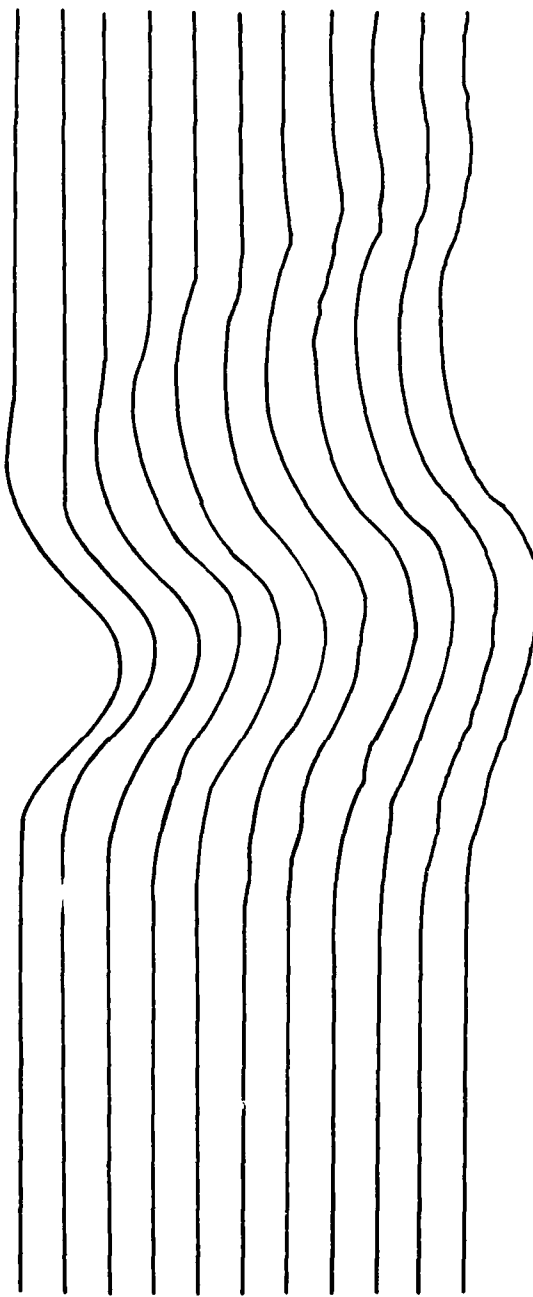


Figure 19. Time sequence for the frontal position for the Sargasso Sea long wavelength, 30 km amplitude test. Time advances to the right at one inertial period intervals.

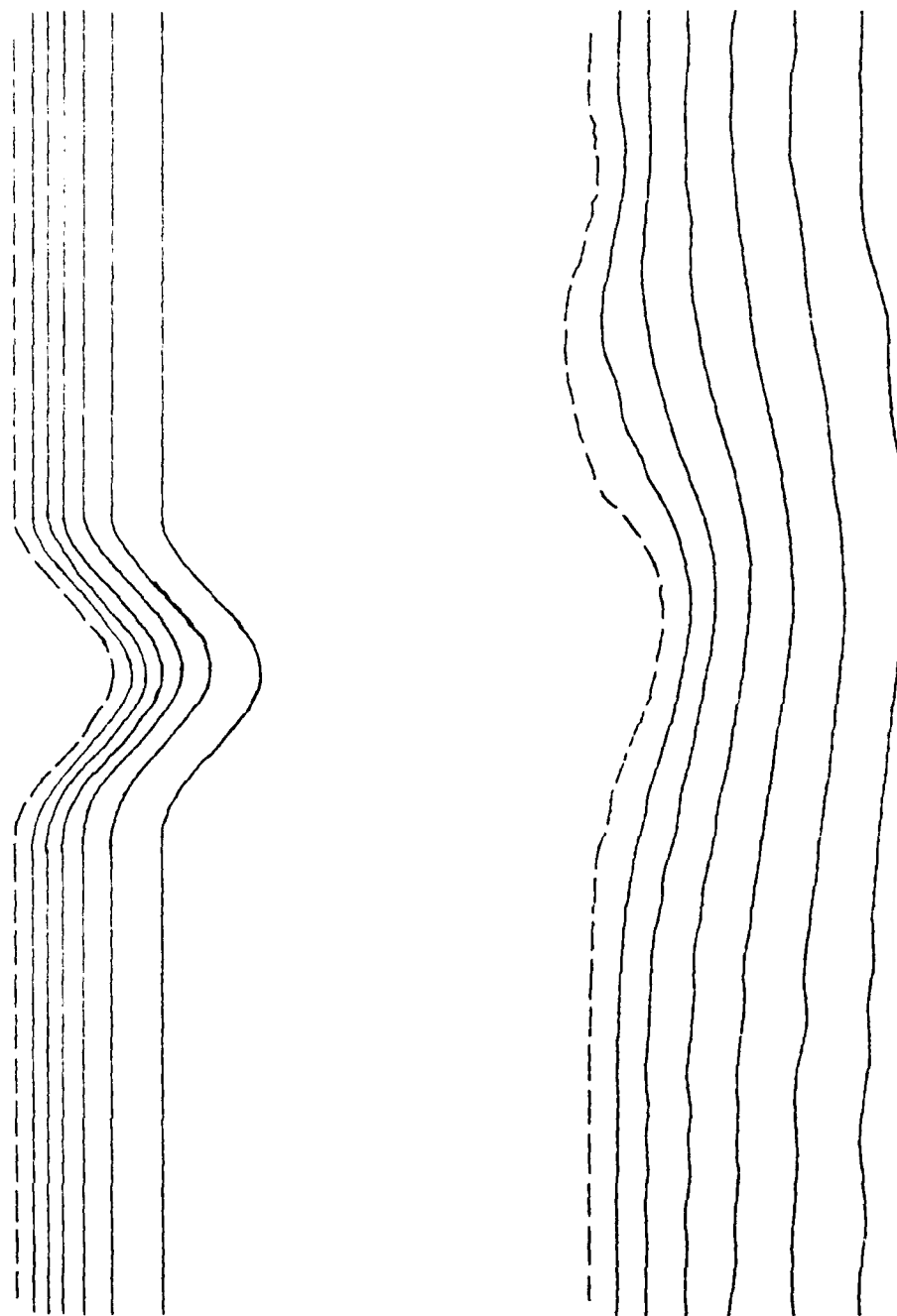


Figure 20. Depth contours for the Sargasso Sea long wavelength, 30 km amplitude test. Plots are for the initial and final (after ten inertial periods) states.

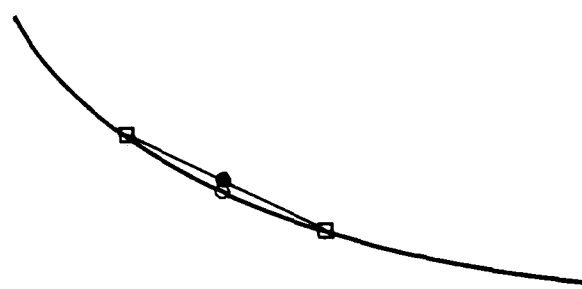
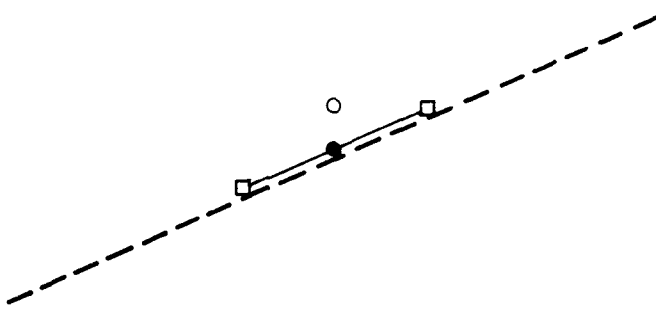


Figure 21. Effect of smoothing a) linear profile,
b) exponential profile.